Structural Engineering and Mechanics, *Vol. 75, No. 3 (2020) 339-356*
DOI: https://doi.org/10.12989/sem.2020.75.3.339

Peridynamic analysis of dynamic fracture behaviors in FGMs with different gradient directions

Miaomiao Kou[1, 2a], Jing Bi[3b], Binhang Yuan[4c] and Yunteng Wang[*5]

[1]*School of Civil Engineering, Qingdao University of Technology, Qingdao, 266033, China*
[2]*Cooperative Innovation Center of Engineering Construction and Safety in Shandong Blue Economic Zone, Qingdao, 266033, China*
[3]*School of Civil Engineering, Guizhou University, Guiyang, 550000, China*
[4]*Computer Science Department, Rice University, 6100 Main Street, Houston, Texas, USA*
[5]*Chongqing University, Chongqing, 400045, China*

(Received November 22, 2019, Revised February 17, 2020, Accepted February 21, 2020)

Abstract. In this article, a developed bond-based peridynamic model for functionally graded materials (FGMs) is proposed to simulate the dynamic fracture behaviors in FGMs. In the developed bond-based peridynamic model for FGMs, bonds are categorized into three different types, including transverse directionally peridynamic bond, gradient directionally peridynamic bond and arbitrary directionally peridynamic bond, according to the geometrical relationship between directions of peridynamic bonds and gradient bonds in FGMs. The peridynamic micromodulus in the gradient directionally and arbitrary directionally peridynamic bonds can be determined using the weighted projection method. Firstly, the standard bond-based peridynamic simulations of crack propagation and branching in the homogeneous PMMA plate are performed for validations, and the results are in good agreement with the previous experimental observations and the previous phase-field numerical results. Then, the numerical study of crack initiation, propagation and branching in FGMs are conducted using the developed bond-based peridynamic model, and the influence of gradient direction on the dynamic fracture behaviors, such as crack patterns and crack tip propagation speed, in FGMs is systematically studied. Finally, numerical results reveal that crack branching in FGMs under dynamic loading conditions is easier to occur as the gradient angle decreases, which is measured by the gradient direction and direction of the initial crack.

Keywords: crack propagation; crack branching; FGMs; gradient direction; bond-based peridynamics

1. Introduction

The functionally graded material, as a multifunctional inhomogeneous composites formed by two or more materials, has been widely applied to manufacture actuators, sensors, transducers, structural member, etc. (Arioui *et al*. 2018, Arefi 2015, Park *et al*. 2016, Galeban *et al*. 2016) and has gradually attracted many research attentions during the last three decades (Nabil *et al*. 2017, Nguyen and Tran 2018, Fallahnejad *et al*. 2018, Jrad *et al*. 2018, Messaoudi *et al*. 2018). The main characteristics of functionally graded materials is that the material properties, such as elastic modulus, Poisson's ratio, fracture energy release rate, etc., and volume fractions smoothly and continuously vary in one or more desired directions (Gu and Asaro 1997, Cheng *et al*. 2018, 2019). The main advantages of functionally graded materials includes alleviating stress concentrations, reducing thermal stress and residual stress, improving fracture toughness enhancing bonded strength and optimizing the mechanical responses under different loading conditions (Arioui *et al*. 2018, Arefi *et al*. 2015, Messaoudi *et al*. 2018, Cheng *et al*. 2019). In fact, at the designing stage of producing processes, some defects and cracks inevitably occur in the functionally graded materials. During the serving process of functionally graded materials, components of functionally graded materials are often subjected to mechanically dynamic or shock loads, which will induce stress concentrations and will result in the initiation, propagation and coalescence of cracks, and ultimate failure of functionally graded materials. Therefore, it is important to investigate the dynamic fracture behaviors of functionally graded materials under mechanically shock loading conditions in the optimizing design and safe utilization of functionally graded components.

In the past decades, numerous researches have been conducted to investigate the dynamic fracture behaviors of functionally graded materials using experimental methods, analytical approaches and numerical methods.

For the experimental approaches, the quasi-static mixed-mode crack initiation and growth in FGM were experimentally studied through fracture experiments by Abanto-Bueno and Lambros (2002). Similarly, the quasi-static mixed-mode crack propagation in a FGM beam under offset loading were experimentally investigated by Jin *et al*. (2009). They presented a detailed experimental study to understand the dynamic fracture behavior of FGMs. The dynamic fracture characteristics of FGMs specimen

*Corresponding author, Ph.D., Post-doctoral Fellow
E-mail: yunteng.wang@kaust.edu.sa; wangyt@cqu.edu.cn
[a] Ph.D., Associate Professor
[b] Ph.D.
[c] Ph.D.

ISSN: 1225-4568 (Print), 1598-6217 (Online)

consisting of compositionally graded glass-filled epoxy plates with initial edge-cracks along the material gradient were researched using the mixed-mode dynamic fracture experiments by Kirugulige and Tippur (2006). Rousseau and Tippur (2001) performed an experimental study of the crack-tip deformation and fracture parameter histories in compositionally graded glass-filled epoxy under low velocity impact loading.

For the analytical approaches, Cheng *et al*. (2012) studied the interface crack of two dissimilar bonded functionally graded strips with arbitrary distributed properties under plane deformations using analytical method. Pan *et al*. (2015) used the analytical method to investigate the effects of the nonhomogeneity constants and geometric parameters on the stress intensity factors (SIFs) for collinear cracks in functionally graded materials with general mechanical properties. Aizikovich *et al*. (2015) developed the semi-analytical solution for mode I penny-shaped crack in soft inhomogeneous layer. Gupta *et al*. (2018) applied the analytical approaches to study the effect of crack location on vibration analysis of partially cracked isotropic and FGM micro-plate with non-uniform thickness. Boujadjra *et al*. (2018) investigated the bending response of FGM plate using a new quasi 3D shear deformation theory to reveal the effect of microstructures in FGMs.

As the computer technique rapidly develops, numerical method gradually becomes an efficient tool to study fracture characteristics in solids under different loading conditions. Compared with the experimental tests, numerical simulations are rarely expensive and can provide physical insights of various fracturing phenomena, which may be difficult to observe and obtain from the laboratory experiments since the monitoring techniques are limited. Finite element methods (FEM) with efficient remeshing techniques (Areias *et al*. 2013), extended finite element method (XFEM) (Moës *et al*. 1999,2002), phase field (Francfort and Marigo 1998, Bourdin *et al*. 2000, Miehe *et al*. 2010, Carlsson and Isaksson 2019), model based on the screened Poisson equation (Areias *et al*. 2016, 2018) and specific meshfree method (Rabczuk and Zi 2007) and cracking particle method (CPM) (Rabczuk and Belytschko 2004, 2007) were developed to study different fracture problems in homogeneous and inhomogeneous solids. Although the aforementioned numerical methods have successfully simulated the crack initiation, crack propagation and crack coalescence in homogeneous and composite solids, there still exist some disadvantages in the previous numerical methods (Kou 2019a, b, c).

Peridynamic theory is based on the nonlocal continuous mechanics, which was proposed by Silling (Kou *et al*. 2019a, b, c) to solve the discontinuous problems in solids. In the peridynamic theory, each material point is interacted with the other material points within a certain region around it via peridynamic bonds. The interactions between material points in the peridynamic theory occur not only at the local regions, but also happen at the nonlocal regions (Silling 2005). The main characteristic of peridynamic theory is that the differential governing equation of motions in the classical continuum is replaced by the integral-differential equation without any spatial derivatives, which leads to the continuous behaviors at crack surfaces and results in overcoming the singularities at crack tips. The other important feature of peridynamics is the introduction of a length parameters, named as horizon, which specifies the size of the region where nonlocal interactions take place. The horizon, which can be regarded as the radius of a circle in two-dimensional cases and of a sphere in three-dimensional cases, can be associated to the characteristic length-scale of materials or the considered phenomenon (Bobaru and Hu 2012, Chen *et al*. 2019, Chen and Bobaru 2015, Chen *et al*. 2016, Silling 2014, Shojaei *et al*. 2016, 2018, Ni *et al*. 2019). Due to the characteristics of peridynamic theory, this numerical methodology is well suited for simulating the initiation, propagation, branching and coalescences of cracks in solid mechanics, especially in situations where the crack paths is not known in advance (Cheng *et al*. 2015). In addition, Wang *et al* (2019a) pointed out that the effective constitutive equations of inhomogeneous materials are nonlocal and can be described by the peridynamic formulation which has some special elastodynamic characteristics (Wang *et al*. 2019b, Wang and Wang 2019).

In spite of limitation of the fixed Poisson's ratio in the version of bond-based peridynamics (Silling *et al*. 2007), the simplest mathematics formulations of bond-based peridynamics allow it to wide applications in different fields. Some scholars applied the bond-based peridynamic model to simulate the transient heat conduction (Bobaru and Duangpanya 2010, 2012, Wang *et al*. 2018a, Bazazzadeh *et al*. 2018, 2020) and thermomechanical fracture problems (Wang *et al*. 2018b, c, d, 2019c, Wang and Zhou 2019). Bobaru and his coworker also studied the dynamic fracture and branching characteristics in homogenous materials (Ha and Bobaru 2010, 2011), and pitting corrosion (Chen and Bobaru 2015). Madenci and his coworker developed the bond-based peridynamic model to study the static and dynamic fracture behaviors (Hu and Madenci 2016, 2017, Hu *et al*. 2017). The nucleation and propagation of cracks in crystal solids were also numerically investigated (Luo *et al*. 2018, Luo and Sundararaghavan 2018). Hong and his coworker developed the bond-based peridynamic model to simulate crack initiation, propagation and coalescence in rock-like materials under compression (Ha *et al*. 2015, Wang *et al*. 2016, Wang *et al*. 2017, Lee *et al*. 2017).

Some scholars have tried to improve the computational ability of bond-based peridynamics from different aspects. Huang *et al*. (2015 a, b) implemented the kernel functions into the bond-based peridynamic model to solve the quasi-static and dynamic fracture problems. Ren *et al*. (2016, 2017) proposed the dual-horizon bond-based peridynamics to overcome the occurrence of ghost forces. The adaptive coupled bond-based peridynamic model with the finite element method (and finite point method) to study dynamic fracture problems in homogeneous brittle solids (Shojaei *et al*. 2016, 2018, 2019a). Wang *et al*. (2017, 2018) developed the two-dimensional and three-dimensional conjugated bond-pair-based peridynamic model to study fracture problems in brittle solids, which overcome the limitation of fixed Poisson's ratio. Moreover, Wang *et al*. (2019d) has applied the conjugated bond-pair-based peridynamic model

to investigate the crack propagation and coalescence process in rock-like materials under compressive-shear loading. A bond-based micropolar peridynamic model with shear deformability was proposed by Diana and Casolo (2019) to study elastic deformation, failure properties and initial yield conditions. Ni *et al*. (2018) developed the bond-based peridyanmic model with irregular distributions for quasi-static fracture problems.

To authors' best knowledge, bond-based peridynamic model for FGMs has been applied to the study quasi-static fracture problems (Cheng *et al*. 2015) and dynamic fracture problems (Cheng *et al*. 2018, 2019) using the simple average numerical method to determine the bond-based peridynamic constants. However, the researches on FGMs using bond-based peridynamic model are still infrequent. In this paper, the main academic contributions of bond-based peridynamic methodology for functionally graded materials under dynamic loading conditions can be classified into two parts. The first contribution is to propose a developed bond-based peridynamic model for functionally graded materials. In the developed bond-based peridynamic model, the bond within one horizon can be classified into transverse directionally peridynamic bond, gradient directionally peridynamic bond and arbitrary directionally peridynamic bond based on the geometrical relationship between bonds' direction and gradient direction in FGMs. The developed bond-based peridynamic model is applied to simulate dynamic fracture behaviors in homogeneous materials. Compared with the previous experimental observations and phase-field results, the present numerical results show good agreements. The second contribution of this study is investigations on the influences of gradient directions on the dynamic fracture behaviors in FGMs. Meanwhile, the dynamic fracture characteristics in FGMs are discussed compared with ones in the homogeneous materials.

This paper is organized as follows: the bond-based peridynamic methodology for functionally graded materials is stated in Section 2. Numerical validation of the bond-based peridynamic model for homogeneous PMMA plates subjected to dynamic loads are performed in Section 3. The directional influence of material properties on dynamic fracturing behaviors of FGMs plates under dynamic loading conditions is investigated in Section 4. Conclusions are drawn in Section 5.

2. Peridynamics for FGMs

2.1. Governing equations of motion

The peridynamic theory is a nonlocal continuum theory which describes the kinematics of an elastic body occupying a region $\mathfrak{B}_0 \subset \mathbb{R}^3$ in its undeformed configuration and $\mathfrak{B}_t \subset \mathbb{R}^3$ in the deformed configuration. The schematic of an elastic body is depicted in Fig. 1. The material point $\mathbf{x}$ interacts with its neighboring point $\mathbf{x}'$ within a region with a finite distance δ, named as horizon, i.e.,

$$\mathcal{H}(\mathbf{x}) := \{(\mathbf{x}' - \mathbf{x}) \in \mathbb{R}^3 | |\mathbf{x}' - \mathbf{x}| \leq \delta\} \tag{1}$$

The relative position vector between two interaction material points $\mathbf{x}$ and $\mathbf{x}'$ is named as bond vector $\boldsymbol{\xi}$. Furthermore, the deformed bond between two interaction material points $\mathbf{y}$ and $\mathbf{y}'$ is described by the relative displacement vector $\boldsymbol{\eta}$ in the deformed configuration. The relative position vector, i.e., bond vector, and the relative displacement vector are respectively defined in the following forms.

$$\boldsymbol{\xi} = \mathbf{x}' - \mathbf{x} \tag{2}$$

$$\boldsymbol{\eta} = \mathbf{u}'(\mathbf{x}', t) - \mathbf{u}(\mathbf{x}, t) \tag{3}$$

where $\mathbf{u}$ and $\mathbf{u}'$ are the displacements at two interacting material points $\mathbf{x}$ and $\mathbf{x}'$

The bond-based peridynamic equations of motion in the computational domain can be written as (Silling 2000, Silling and Askari 2005)

$$\rho(\mathbf{x}) \frac{\partial^2 \mathbf{u}(\mathbf{x}, t)}{\partial t^2} = \int_{\mathcal{H}(\mathbf{x})} \boldsymbol{f}(\boldsymbol{\eta}, \boldsymbol{\xi}, t) dV_{\mathbf{x}'} + \boldsymbol{b}(\mathbf{x}, t) \tag{4}$$

in which ρ is the mass density, $\boldsymbol{f}$ denotes the long-range pairwise force density and $\boldsymbol{b}$ represents the externally applied body force density.

As stated by Silling and Askari (2005) and Cheng *et al*. (2018, 2019), the long-range pairwise force density $\boldsymbol{f}(\boldsymbol{\eta}, \boldsymbol{\xi}, t)$ can be derived by microscopic potential $\omega(\boldsymbol{\eta}, \boldsymbol{\xi}, t)$ at time t. The microscopic potential $\omega(\boldsymbol{\eta}, \boldsymbol{\xi}, t)$ in the materials is dependent on the linearly relative elongation magnitude, i.e., bond stretch, and the microscopic potential $\omega(\boldsymbol{\eta}, \boldsymbol{\xi}, t)$ in the materials can read

$$\omega(\boldsymbol{\eta}, \boldsymbol{\xi}, t) = \frac{1}{2} c(\|\boldsymbol{\xi}\|, \delta) s^2 \|\boldsymbol{\xi}\| \tag{5}$$

where $c(\|\boldsymbol{\xi}\|, \delta)$ is the micromodulus function, s is the scalar representing the bond stretch, and $\|\boldsymbol{\xi}\|$ is the length of a bond.

The stretch of a bond can be expressed as

$$\mathrm{s} = \frac{\|\boldsymbol{\xi} + \boldsymbol{\eta}\| - \|\boldsymbol{\xi}\|}{\|\boldsymbol{\xi}\|} \tag{6}$$

where $\|\boldsymbol{\xi}\|$ is the length of a bond in the undeformed configuration and $\|\boldsymbol{\xi} + \boldsymbol{\eta}\|$ stands for the length of a deformed bond in the deformed configuration.

Then, the pairwise force density can be derived from a microscopic elastic potential $\omega(\boldsymbol{\eta}, \boldsymbol{\xi}, t)$ in the following form.

$$\boldsymbol{f}(\boldsymbol{\eta}, \boldsymbol{\xi}, t) = \frac{\partial \omega(\boldsymbol{\eta}, \boldsymbol{\xi}, t)}{\partial \boldsymbol{\eta}} = c(\|\boldsymbol{\xi}\|, \delta) s \frac{\boldsymbol{\xi} + \boldsymbol{\eta}}{\|\boldsymbol{\xi} + \boldsymbol{\eta}\|} \tag{7}$$

where the term $\boldsymbol{\xi} + \boldsymbol{\eta}/\|\boldsymbol{\xi} + \boldsymbol{\eta}\|$ denotes the unit vector of a deformed bond in the deformed configuration.

In the original bond-based peridynamic model (Silling 2000, Silling and Askari 2005), the micromodulus function $c(\|\boldsymbol{\xi}\|, \delta)$ is reduced to the form $c(\delta)$, which ignores the effect of distance between two interacting material points on the microscopic elastic stiffness of the bond (Huang *et al*. 2015a, b, Gu *et al*. 2016). In the present study, the improved micromodulus $c(\|\boldsymbol{\xi}\|, \delta)$ proposed by Huang *et al*. (2015a, b) and Gu *et al*. (2016) is adopted to construct

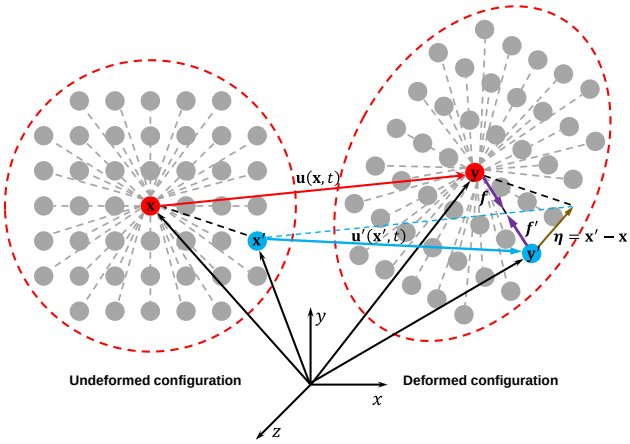

Fig. 1 A schematic of bond-based peridynamic model in the undeformed and deformed configurations

the developed bond-based peridynamics for FGMs. The improved micromodulus $c(\|\boldsymbol{\xi}\|, \delta)$ can be written as

$$c(\|\boldsymbol{\xi}\|, \delta) = c(0, \delta)\mathrm{g}(\|\boldsymbol{\xi}\|, \delta) \tag{8}$$

where $\mathrm{g}(\|\boldsymbol{\xi}\|, \delta)$ is the kernel function, which reflects the distribution of the intensity of long-range force density in materials. The kernel function can be expressed as

$$\mathrm{g}(\|\boldsymbol{\xi}\|, \delta) = \begin{cases} \left(1 - \left(\dfrac{\|\boldsymbol{\xi}\|}{\delta}\right)^2\right)^2 & \|\boldsymbol{\xi}\| \le \delta \\ 0 & \|\boldsymbol{\xi}\| > \delta \end{cases} \tag{9}$$

where δ stands for the horizon size.

By establishing the equivalent relationship between the macroscopic strain energy density based on the classical continuum mechanics and the microscopic strain energy density on the basis of peridynamic theory, the improved micromodulus in the bond-based peridynamic model can be written in the following form (Huang *et al*. 2015a, b, Gu *et al*. 2016)

$$c(\|\boldsymbol{\xi}\|, \delta) = \frac{315E}{8\pi\delta^3}\left(1 - \left(\frac{\|\boldsymbol{\xi}\|}{\delta}\right)^2\right)^2 \tag{10}$$

where E is the Young's modulus of materials.

To calculate the critical stretch of a bond for determining fracture surface in materials, the peridynamic critical energy density stored in a bond is obtained by summing the energy required to create unit fracture area in peridynamics and equating it to the energy release rate. According to Silling and Askari (Silling and Askari 2005), to open a fracture surface of; unit area, the energy released to break all the bonds connecting each point along $0 \le \mathrm{z} \le \delta$ to its neighbor point in the cylindrical cap for two-dimensional analysis (see Fig. 2) across the fracture surface is summed as

$$\mathcal{G}_0 = 2\int_0^{\delta}\int_z^{\delta}\int_0^{\arccos\left(\frac{z}{\|\boldsymbol{\xi}\|}\right)}\left[\frac{c(\|\boldsymbol{\xi}\|, \delta)s^2\|\boldsymbol{\xi}\|}{2}\right]\|\boldsymbol{\xi}\| d\,\theta d\|\boldsymbol{\xi}\| dz \tag{11}$$

The aforementioned integral, when evaluated and solved for the critical stretch of a bond, we can obtain

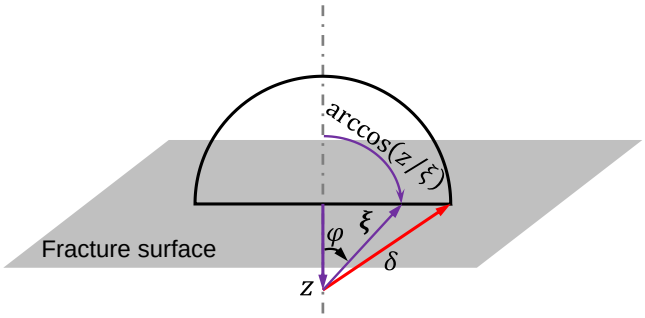

Fig. 2 The schematic of evaluating strain energy release rate in bond-based peridynamic model.

$$s_0 = \sqrt{\frac{1024\pi\mathcal{G}_0}{7(120\pi - 133)E\delta}} \tag{12}$$

Accordingly, the historical function is adopted to describe the state of a bond, which is expressed as

$$\chi(\boldsymbol{\xi}, t) = \begin{cases} 0 & s \ge s_0 \\ 1 & s < s_0 \end{cases} \tag{13}$$

Then, in a peridynamic formulation of solid mechanics, material failure is modeled through a scalar field referred as damage defined as the fraction of broken bonds at a material point in its horizon

$$\varphi(\mathbf{x}, t) = 1 - \frac{\int_{\mathcal{H}(\mathbf{x})}\chi(\boldsymbol{\xi}, t)dV_{\mathbf{x}'}}{\int_{\mathcal{H}(\mathbf{x})}dV_{\mathbf{x}'}} \tag{14}$$

The value of damage index $\varphi(\mathbf{x}, t)$ changes from zero to one. When $\varphi(\mathbf{x}, t)$ is equal to one, it represents all the bonds attached to a point broken. However, when $\varphi(\mathbf{x}, t)$ equates to zero, it represents the intact materials.

2.2. Bond-based peridynamic model for FGMs

In the developed bond-based peridynamic model for FGMs, bonds are categorized into three different types, including transverse directionally peridynamic bond, gradient directionally peridynamic bond and arbitrary directionally peridynamic bond, according to the geometrical relationship between directions of peridynamic bonds and gradient bonds in FGMs, as shown in Fig. 3.

To accurate determine the peridynamic bond type, the directional angle between bond directional vector and functionally graded directional vector is taken into consideration. The directional angle ϑ can be obtained by using the following equation.

$$\vartheta = \cos^{-1}\frac{\boldsymbol{\xi}\cdot\boldsymbol{n}_{\mathrm{FGMs}}}{\|\boldsymbol{\xi}\| \times \|\boldsymbol{n}_{\mathrm{FGMs}}\|} \tag{15}$$

in which $\boldsymbol{\xi}$ is the bond vector between two interacting material point within one horizon, $\boldsymbol{n}_{\mathrm{FGMs}}$ denotes the functionally graded directional vector, as shown in Fig. 3.

Based on the calculated value of the directional angle, gradient directionally peridynamic bond, transverse directionally peridynamic bond and arbitrary directionally peridynamic bond are respectively determined as follows

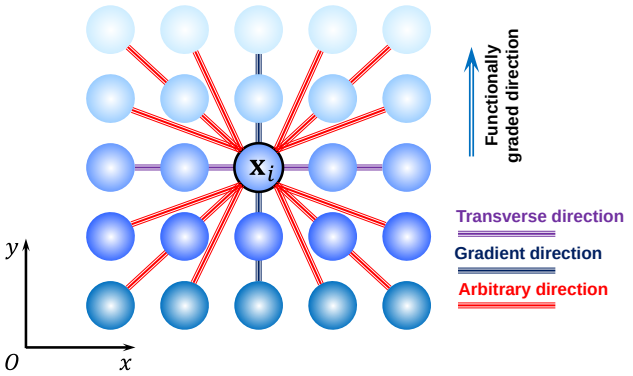

Fig. 3 Interactions of a family of material points for the functionally graded materials

$$\vartheta = 0° \quad \text{Gradient directionally bond} \tag{16a}$$

$$\vartheta = 90° \quad \text{Transverse directionally bond} \tag{16b}$$

$$\vartheta \neq 0° \text{ and } \vartheta \neq 90° \quad \text{Arbitrary directionally bond} \tag{16c}$$

2.2.1 Gradient directionally peridynamic bond

For the gradient directionally peridynamic bond connecting two interacting points $\mathbf{x}$ and $\mathbf{x}'$ in FGMs, as shown in Fig. 3, the micromodulus of the gradient directionally peridynamic bond can be evaluated by the average values of material properties at two interacting points $\mathbf{x}$ and $\mathbf{x}'$, which is same as the previous research (Cheng *et al*. 2015). Similarly, the critical energy release rate also can be evaluated using the simple average techniques. Therefore, the Young's modulus $E_G(\mathbf{x},\mathbf{x}')$ and critical fracture energy release rate $\mathcal{G}_{G0}(\mathbf{x},\mathbf{x}')$ in the gradient directionally peridynamic bond can be respectively determined as follows:

$$E_G(\mathbf{x},\mathbf{x}') = \frac{E(\mathbf{x}) + E(\mathbf{x}')}{2} \tag{17a}$$

$$\mathcal{G}_{G0}(\mathbf{x},\mathbf{x}') = \frac{\mathcal{G}_0(\mathbf{x}) + \mathcal{G}_0(\mathbf{x}')}{2} \tag{17b}$$

Based on Eq. (10), the micromodulus at the gradient directionally peridynamic bond c_G can be expressed in the following form.

$$c_G = \frac{315E_G(\boldsymbol{x},\boldsymbol{x}')}{8\pi\delta^3}\left(1-\left(\frac{\|\boldsymbol{\xi}\|}{\delta}\right)^2\right)^2 \tag{18}$$

Similarly, according to Eq. (12), the critical stretch of a gradient directionally peridynamic bond s_{G0} can be written as follows:

$$s_{G0} = \sqrt{\frac{1024\pi\mathcal{G}_{G0}(\boldsymbol{x},\boldsymbol{x}')}{7(120\pi-133)E_G(\boldsymbol{x},\boldsymbol{x}')\delta}} \tag{19}$$

2.2.2 Transverse directionally peridynamic bond

For the transverse directionally peridynamic bond due to interactions between material points $\mathbf{x}$ and $\mathbf{x}'$ in FGMs, as shown in Fig. 3, material properties, such as Young's modulus and critical energy release rate, are same with each other. Thus, the Young's modulus $E_T(\mathbf{x},\mathbf{x}')$ and critical energy release rate $\mathcal{G}_{T0}(\mathbf{x},\mathbf{x}')$ in the transverse directionally peridynamic bond can be respectively written in the following forms.

$$E_T(\mathbf{x},\mathbf{x}') = E(\mathbf{x}) = E(\mathbf{x}') \tag{20a}$$

$$\mathcal{G}_{T0}(\mathbf{x},\mathbf{x}') = \mathcal{G}_0(\mathbf{x}) = \mathcal{G}_0(\mathbf{x}') \tag{20b}$$

Based on Eq. (10), the micromodulus at a transverse directionally peridynamic bond c_T can be expressed in the following form.

$$c_T = \frac{315E_T(\mathbf{x},\mathbf{x}')}{8\pi\delta^3}\left(1-\left(\frac{\|\boldsymbol{\xi}\|}{\delta}\right)^2\right)^2 \tag{21}$$

Similarly, according to Eq. (12), the critical stretch of a transverse directionally peridynamic bond s_{T0} can be written as follows:

$$s_{T0} = \sqrt{\frac{1024\pi\mathcal{G}_{T0}(\mathbf{x},\mathbf{x}')}{7(120\pi-133)E_T(\mathbf{x},\mathbf{x}')\delta}} \tag{22}$$

2.2.3 Arbitrary directionally peridynamic bond

For the arbitrary directionally peridynamic bond connected to two interacting material points $\mathbf{x}$ and $\mathbf{x}'$, it is important to determine the corrected Young's modulus and corrected critical energy release rate for simulating the mechanical behaviors of FGMs in the framework of peridynamics. The weighted projection method is firstly used to establish the projected length of arbitrary directionally peridynamic bond on the functionally gradient directions, as shown in Fig. 3. Then, the projected length of arbitrary directionally peridynamic bond on the functionally gradient directions in FGMs is applied to determine the corrected Young's modulus $E_A(\mathbf{x},\mathbf{x}')$ and corrected critical energy release rate $\mathcal{G}_{A0}(\mathbf{x},\mathbf{x}')$ in the following forms, respectively.

$$E_A(\mathbf{x},\mathbf{x}') = \frac{E(\mathbf{x})\cdot\|\xi_{\mathbf{x}\mathbf{x}'}\| + E(\mathbf{x}')\cdot\|\xi_{\mathbf{x}\mathbf{x}'}\|}{2\|\xi_{\mathbf{x}\mathbf{x}'}\|\cos\vartheta} \quad \vartheta \neq 90° \tag{23a}$$

$$\mathcal{G}_{A0}(\mathbf{x},\mathbf{x}') = \frac{\mathcal{G}_0(\mathbf{x})\cdot\|\xi_{\mathbf{x}\mathbf{x}'}\| + \mathcal{G}_0(\mathbf{x}')\cdot\|\xi_{\mathbf{x}\mathbf{x}'}\|}{2\|\xi_{\mathbf{x}\mathbf{x}'}\|\cos\vartheta} \quad \vartheta \neq 90° \tag{23b}$$

where ϑ is the directional angle determined by the unit directions of arbitrary bond vector and functionally gradient direction in FGMs.

It can be observed from Eq. (23a) and Eq. (23b), the formulations of arbitrary directionally peridynamic bond can be simplified into the ones of gradient direction peridynamic bond, which is same as the formulation proposed by Cheng *et al*. (2015). However, Eq. (23a) and Eq. (23b) cannot be simplified to describe the case of the transverse directionally peridynamic bond, i.e., $\vartheta = 90°$, since the weighted projection method is adopted.

Based on Eq. (10), the micromodulus at a transverse

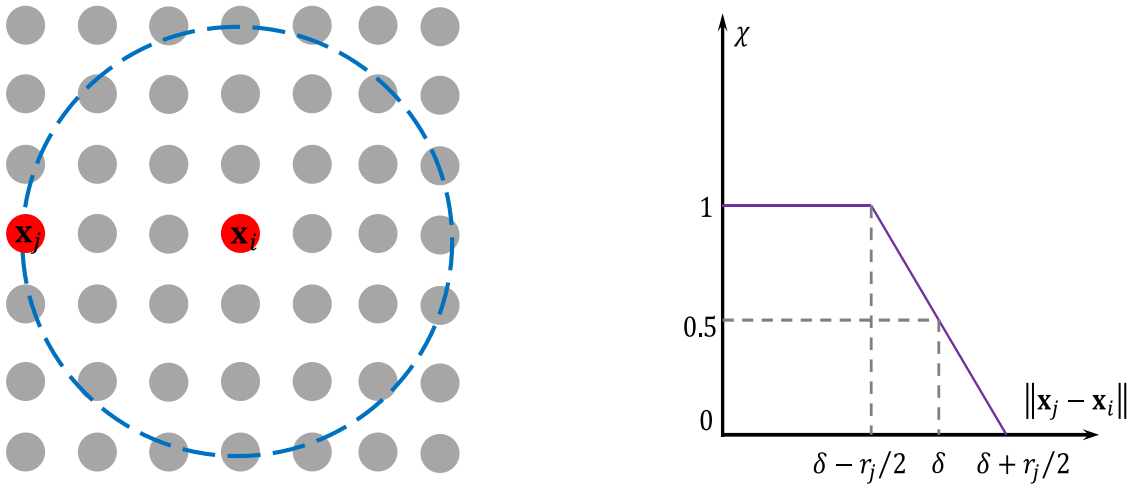

(a) (b)

Fig. 4 The schematic of volumetric technique for surface corrections in peridynamics: (a) two-dimensional diagram for discrete material particles with boundaries and (b) volume fracture as a function of distance (modification based on Le *et al.* (2014))

directionally peridynamic bond c_A can be expressed in the following form.

$$c_A = \frac{315E_A(\mathbf{x},\mathbf{x}')}{8\pi\delta^3}\left(1-\left(\frac{\|\boldsymbol{\xi}\|}{\delta}\right)^2\right)^2 \tag{24}$$

Similarly, according to Eq. (12), the critical stretch of a transverse directionally peridynamic bond s_{T0} can be written as follows:

$$s_{A0} = \sqrt{\frac{1024\pi\mathcal{G}_{A0}(\mathbf{x},\mathbf{x}')}{7(120\pi-133)E_A(\mathbf{x},\mathbf{x}')\delta}} \tag{25}$$

2.3 Damage evolution

In the numerical simulation, the equation of motion for a material particle $\mathbf{x}_{(i)}$, which is uniformly distributed in the FGMs can be expressed as

$$\begin{aligned}\rho_{(i)}\ddot{\mathbf{u}}_{(i)} = &\sum_{j=1}^{N_G}\chi_{G(ij)}\upsilon_{(i)(j)}\boldsymbol{f}_{G(i)(j)}\Delta V_{(j)} \\ &+\sum_{j=1}^{N_T}\chi_{T(ij)}\upsilon_{(i)(j)}\boldsymbol{f}_{T(i)(j)}\Delta V_{(j)} \\ &+\sum_{j=1}^{N_A}\chi_{A(ij)}\upsilon_{(i)(j)}\boldsymbol{f}_{A(i)(j)}\Delta V_{(j)}\end{aligned} \tag{26}$$

where N_G, N_T and N_A are the numbers of material particles, which are used to construct the gradient directionally bond, transverse directionally bond and arbitrary directionally bond with a given material particle $\mathbf{x}_{(i)}$ within its given horizon $\mathcal{H}(\mathbf{x}_{(i)})$, respectively; $\boldsymbol{f}_{G(i)(j)}$, $\boldsymbol{f}_{T(i)(j)}$ and $\boldsymbol{f}_{A(i)(j)}$ are the pairwise force densities in the gradient directionally bond, transverse directionally bond and arbitrary directionally bond, respectively; $\chi_{G(ij)}$, $\chi_{G(ij)}$ and $\chi_{G(ij)}$ are the history functions used to describe the damage histories at gradient, transverse and arbitrary directionally bonds, respectively; and $\upsilon_{(i)(j)}$ is the volume fraction, which is used to approximate the cut-off distance in two-dimensional implementation. The volume fraction $\upsilon_{(i)(j)}$ is approximated by a linearly decreasing function near the neighborhood boundary (Le *et al.* 2014), as shown in Fig. 4.

For the material particles satisfying $\|\mathbf{x}_{(j)} - \mathbf{x}_{(i)}\| \le \delta - \Delta x/2$, the volume fraction function is

$$\upsilon_{(i)(j)} = 1 \tag{27a}$$

For the material particle satisfying $\delta - \Delta x/2 < \|\mathbf{x}_{(j)} - \mathbf{x}_{(i)}\| < \delta + \Delta x/2$, the volume fraction function is

$$\upsilon_{(i)(j)} = \frac{1}{2} + \frac{\delta - \|\mathbf{x}_{(j)} - \mathbf{x}_{(i)}\|}{\Delta x} \tag{27b}$$

where Δx is the material particle spacing and δ is the horizon size.

For the material particle satisfying $\|\mathbf{x}_{(j)} - \mathbf{x}_{(i)}\| \ge \delta + \Delta x/2$, the volume fraction function is

$$\upsilon_{(i)(j)} = 0 \tag{27c}$$

A history dependent failure function, χ, is defined for each interaction to indicate the bond breakage as (Hu and Madenci 2016, 2017, Hu *et al.* 2017)

$$\chi_{G(ij)} = \begin{cases} 1 & s_{(i)(j)} < s_{G0} \\ 0 & s_{(i)(j)} \ge s_{G0} \end{cases} \tag{28a}$$

$$\chi_{T(ij)} = \begin{cases} 1 & s_{(i)(j)} < s_{T0} \\ 0 & s_{(i)(j)} \ge s_{T0} \end{cases} \tag{28b}$$

$$\chi_{A(ij)} = \begin{cases} 1 & s_{(i)(j)} < s_{A0} \\ 0 & s_{(i)(j)} \ge s_{A0} \end{cases} \tag{28c}$$

in which $\chi_{G(ij)}$, $\chi_{T(ij)}$ and $\chi_{A(ij)}$ are related to the gradient directionally bond, transverse directionally bond and arbitrary directionally bond, respectively.

The damage index at a material point $\mathbf{x}_{(i)}$ is represented by local damage parameter as (Silling and Askari 2005)

$$\varphi_{(i)} = 1 - \frac{\sum_{j=1}^{N_G} \chi_{G(ij)} \Delta V_j + \sum_{j=1}^{N_T} \chi_{A(ij)} V_j + \sum_{j=1}^{N_A} \chi_{A(ij)} \Delta V_j}{\sum_{j=1}^{N_{total}} \Delta V_j} \quad (29)$$

2.4 Time integration

In the present study, time integration is performed by means of an explicit Velocity-Verlet scheme (Shojaei *et al*. 2019b, Mossaiby *et al*. 2020) which which is simple, robust and reliable. Displacement, velocity, and acceleration of each particle $\mathbf{x}_{(i)}$ at $t^{(n)}$, i.e., $\left(\mathbf{u}_{(i)}^{(n)} \quad \dot{\mathbf{u}}_{(i)}^{(n)} \quad \ddot{\mathbf{u}}_{(i)}^{(n)}\right)$, can be obtained by the solver proceeding to time $t^{(n+1)} = t^{(n)} + \Delta t$ as

$$\dot{\mathbf{u}}_{(i)}^{(n+1/2)} = \dot{\mathbf{u}}_{(i)}^{(n)} + \frac{\Delta t}{2} \ddot{\mathbf{u}}_{(i)}^{(n)} \quad (30a)$$

$$\mathbf{u}_{(i)}^{(n+1)} = \mathbf{u}_{(i)}^{(n)} + \Delta t \dot{\mathbf{u}}_{(i)}^{(n+1/2)} \quad (30b)$$

$$\dot{\mathbf{u}}_{(i)}^{(n+1)} = \dot{\mathbf{u}}_{(i)}^{(n+1/2)} + \frac{\Delta t}{2} \ddot{\mathbf{u}}_{(i)}^{(n+1)} \quad (30c)$$

where Δt is the constant time step, which has to be taken smaller than the critical time step, $\Delta t_c = \xi_{\min}/c_k$, and $\xi_{\min}$ is the smallest bond length of the computational domain, e.g., $\xi_{\min} = \Delta x$ for a uniform discretization, and c_k is the sound velocity in materials.

Based on Eq. (30), the time integration can advance to the next time step by following equation.

$$\mathbf{u}_{(i)}^{(n+1)} = \mathbf{u}_{(i)}^{(n)} + \Delta t \dot{\mathbf{u}}_{(i)}^{(n)} + \frac{(\Delta t)^2}{2} \ddot{\mathbf{u}}_{(i)}^{(n+1)} \quad (31)$$

Furthermore, the computational flowchart is presented in Fig. 5 to illustrate details of numerical simulations. Due to the classification of three different bonds in the numerical simulations, the computational efficiency of the developed bond-based peridynamic model for FGMs may be lower than that in the previous literature (Cheng *et al*. 2015).

3. Numerical validations

The developed bond-based peridynamic analyses are performed on homogeneous PMMA strip specimen geometries with dimensions, as shown in Fig. 6(a), i.e., $L \times H = 50\,\text{mm} \times 25\,\text{mm}$. The two-dimensional plane stress condition is assumed. The material properties of homogeneous PMMA are listed as follows: Young's modulus $E = 3.25\,\text{GPa}$, Poisson's ratio $\upsilon = 1/3$, mass density $\rho = 1190\ \text{kg/m}^3$, the critical fracture energy release rate $G_c = 200\ \text{J/m}^2$, Rayleigh velocity $c_R = 962\ \text{m/s}$. To illustrate the effect of initial crack length on the dynamic fracture behaviors of homogeneous PMMA strip specimens, two homogeneous PMMA strip specimens with different initial crack lengths: $a_0 = 0.75\,\text{mm}$ and $a_0 = 2.0\,\text{mm}$. A sharp dynamic tensile load, σ_0, is symmetrically applied on the boundary of homogeneous PMMA strip specimens, as shown in Fig. 6(a)-6(b). The magnitude of sharp dynamic tensile load σ_0 is equal to 1.0 MPa.

In the numerical simulations, the peridynamic material particles are uniformly distributed with particle spacing of $\Delta = 0.167\text{mm}$, the nonlocal ratio $m = 4.0$ and horizon size $\delta = 0.668\,\text{mm}$, which recommend by Cheng *et al*. (2015). The time incremental step is adopted as $\Delta t = 2 \times 10^{-8}\,\text{s}$, which is smaller than the critical time step based on CFL conditions (Cheng *et al*. 2015, Ha and Bobaru 2010, 2011).

Fig. 7 shows the dynamic fracture processes of the homogeneous plates containing a pre-existing crack with different initial lengths, i.e., $a_0 = 0.75\,\text{mm}$ and $a_0 = 2.0\,\text{mm}$ under the dynamic loading conditions. It can be found from Fig. 7 that when the initial crack length equates to 2.0 mm, the crack growth path is straight and no crack branching occurs. However, when the initial crack length equates to 0.75 mm, crack branching occurs in the homogeneous plate under the dynamic loading conditions, as shown in Fig. 7. Furthermore, the symmetrical geometrical and loading conditions leads to the symmetrical crack growth paths.

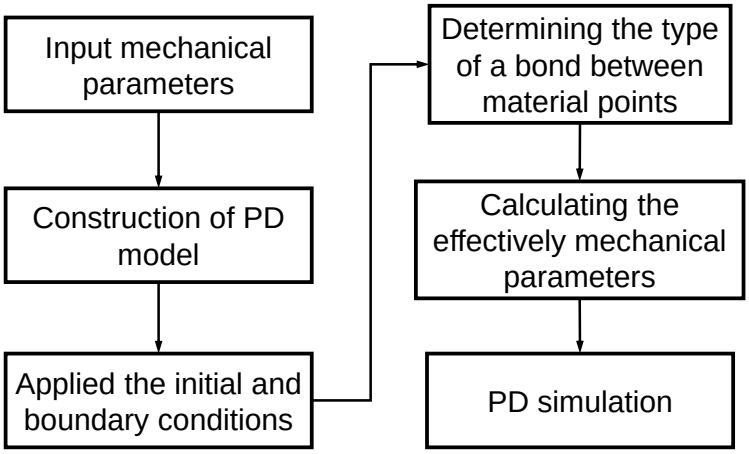

Fig. 5 The computational flowchart of the new developed bond-based peridynamic model

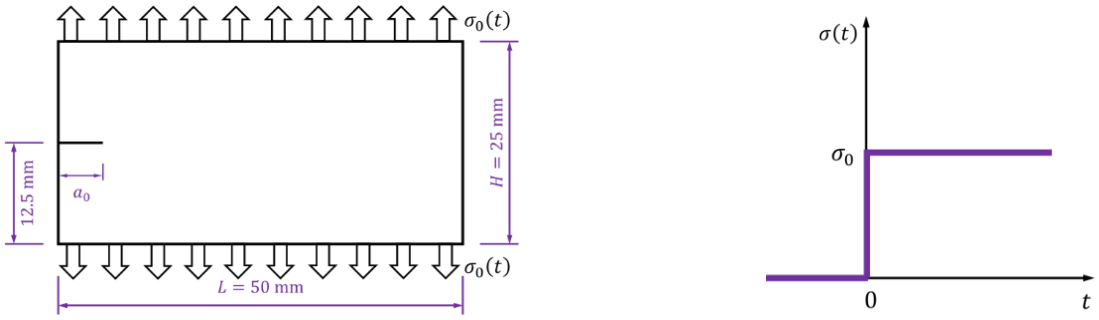

(a) (b)

Fig. 6 (a) Geometrical and boundary conditions of a homogeneous PMMA plate and (b) applied dynamic loads versus time

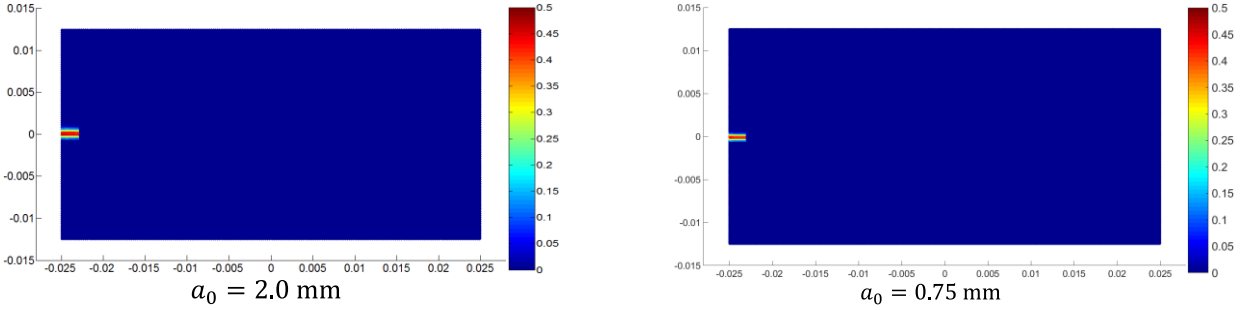

(a) $t = 10$ μs

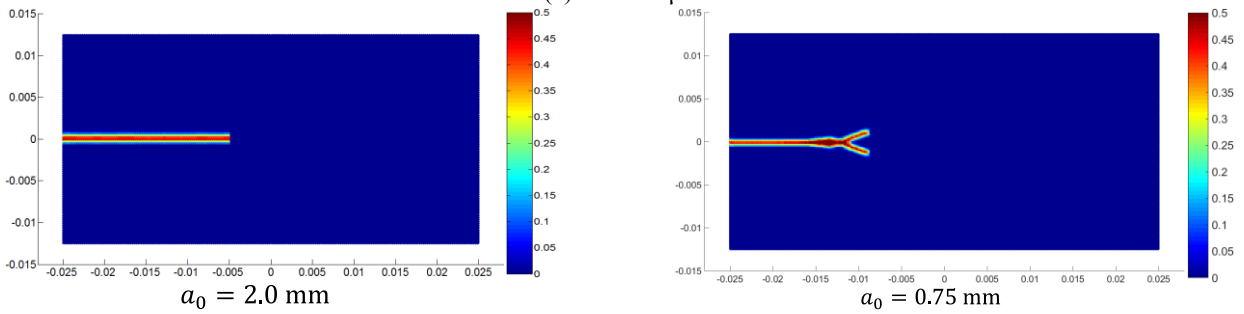

(b) $t = 75$ μs

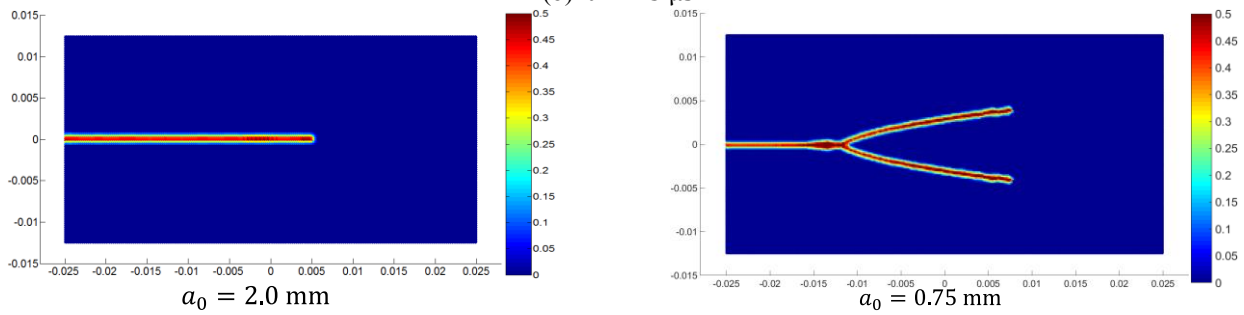

(c) $t = 120$ μs

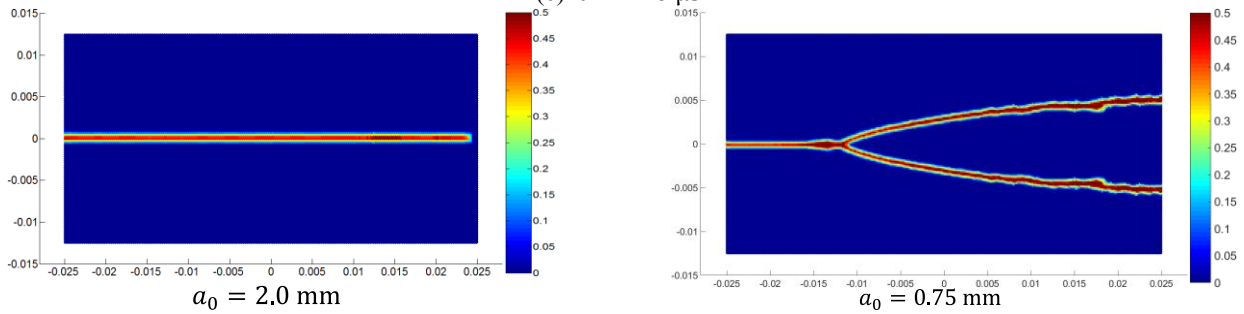

(d) $t = 160$ μs

Fig. 7 Dynamic fracturing process of a homogeneous PMMA plate

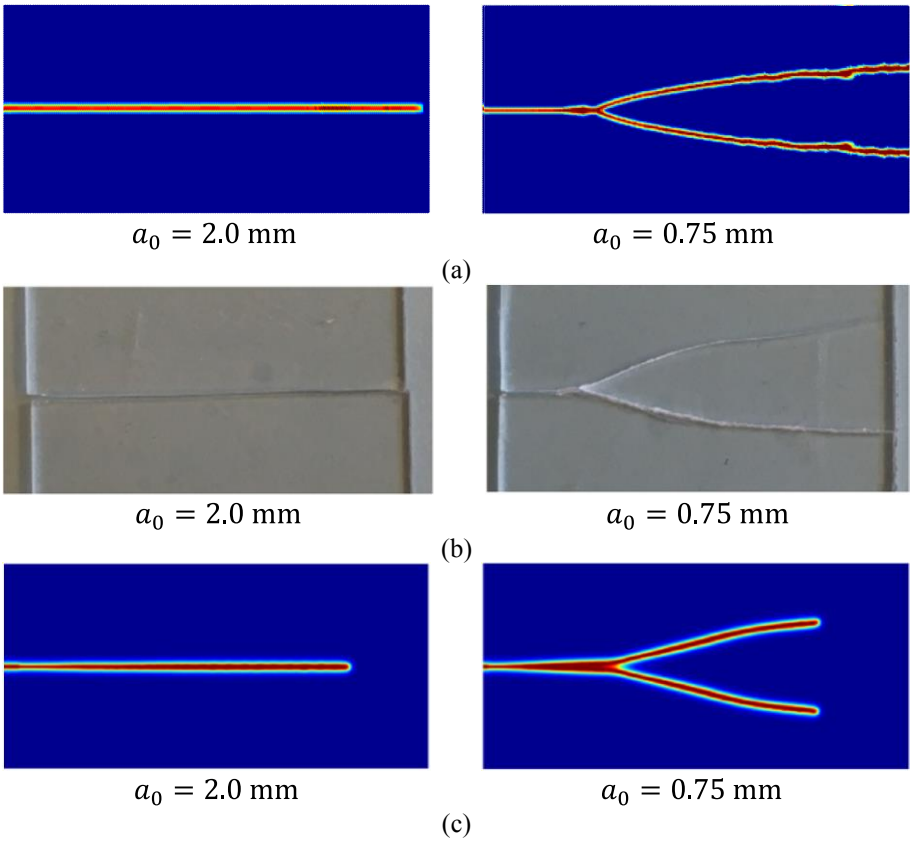

Fig. 8 Comparison of the ultimate dynamic crack paths obtained from (a) the present peridynamic simulations, (b) the previous experimental observations (Carlsson and Isaksson 2019) and (c) the previous phase-field simulations (Carlsson and Isaksson 2019).

Table 1 Computational details of the four numerical homogenous plates

No.	Particle spacing Δ (mm)	Horizon size δ (mm)	Nonlocal ratio m	Numerical of particles
Case-I	0.250	1.000	4.0	200 × 100
Case-II	0.167	0.668		300 × 150
Case-III	0.125	0.500		400 × 200
Case-IV	0.100	0.400		500 × 250

The ultimate dynamic crack growth paths in the PMMA plates with two different kinds of pre-set cracks predicted by the present peridynamic model are compared with the previous experimental (Carlsson and Isaksson 2019) and phase-field results (Carlsson and Isaksson 2019), as shown in Fig. 8. It can be found from Fig. 8 that the present peridynamic crack growth paths are in good agreement with the experimental observations and the numerically predicted crack growth paths by phase field. The good agreement illustrates the effectiveness and accuracy of the proposed numerical model, which can be reproduce the previous dynamic fracture experiments.

To demonstrate the convergence and stability of the developed bond-based peridynamic model, δ-convergence study containing four different numerical samples is conducted. The computational details of four numerical samples are listed in Table 1. The ultimate dynamic crack growth paths in the four numerical homogenous plates are shown in Fig. 9. It can be observed from Fig. 9 that the dynamic crack growth paths are not affected by the decrease of horizon size, which indicates the convergence and stability of the developed bond-based peridynamics.

4. Numerical results and discussions

4.1 Numerical model setup

The FGMs plate with a preexisting crack has the 25 mm height and 50 mm length, and the FGMs plate is subjected to the dynamic loads of $\sigma_0 = 1.0$ MPa on the top and bottome boundaries. The length of the pre-existing crack is equal to 0.75 mm.

In the FGMs, Young's modulus E varies from 3.25 GPa to 10.0 GPa and the critical fracture energy release rate G_c changes from 100 J/m^2 to 200 J/m^2. The FGMs gradient form is adopted as an exponetial function, the following exponentially functional curve fitting are taken into consideration.

$$E_{\mathrm{FGMs}} = E_{\min} \cdot e^{\alpha y \sin\vartheta} \tag{32}$$

$$\mathcal{G}_{\mathrm{FGMs}} = \mathcal{G}_{\min} \cdot e^{\beta y \sin\vartheta} \tag{33}$$

where α and β are two different fitting coefficients, which are expressed as

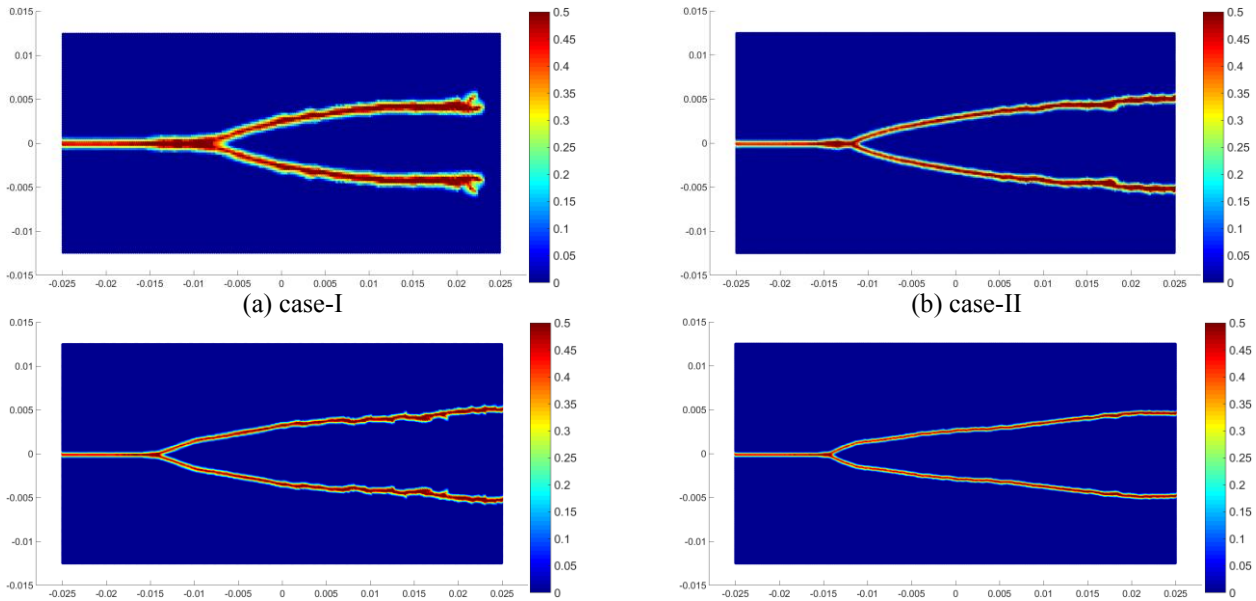

(a) case-I (b) case-II

(c) case-III (d) case-IV

Fig. 9. Ultimately dynamic crack growth paths in the four different numerical PMMA plates

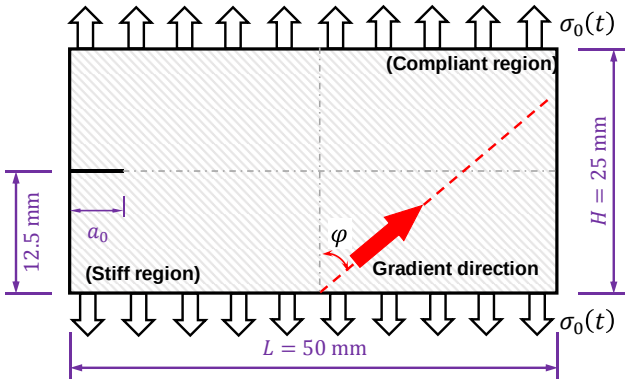

Fig. 10 Geometrical and boundary conditions of FGMs plates with different gradient directions

$$\alpha = \frac{\ln(E_{\min}/E_{\max})}{H/\sin\vartheta} \tag{34}$$

$$\beta = \frac{\ln(\mathcal{G}_{\min}/\mathcal{G}_{\max})}{H/\sin\vartheta} \tag{35}$$

where $E_{\min}$ and $E_{\max}$ are values of Young's modulus in the complaint and stiff regions, respectively; $\mathcal{G}_{\min}$ and $\mathcal{G}_{\max}$ are values of the critical fracture energy release rates in the complaint and stiff regions, respectively; H is the width of the FGMs plate, and φ is the inclination angle of gradient direction, as shown in Fig. 10. Furthermore, the five different numerical models with different gradient directions are shown in Fig. 11.

The other computational parameters are same as the description in Section 3. In the numerical model, PD particles are uniformly distributed with the spacing of 0.25 mm, and the nonlocal size of horizon is equal to 1.0 mm, which means that the nonlocal ratio equates to 4.0.

4.2 Numerical results

The dynamic fracturing process of FGMs plate containing a preexisting crack with the gradient direction of 0° is performed in Fig. 12. It can be found from Fig. 12(a) that the main straight crack is initiated at the pre-existing crack tip and propagates towards the horizontal direction at $t = 10$ μs. As shown in Fig. 12(b), the main straight crack propagates along the oblique direction towards the compliant parts in the FGMs plate at $t = 30$ μs. Furthermore, the main crack splits into two asymmetrical branches, and the two crack branches propagate to the right boundary at $t = 60$ μs. It can be found from Fig. 12(c)-12(d) that the crack branching angle with respect to the central horizontal axis in the compliant parts is larger than that in the stiff parts.

The dynamic fracturing process of FGMs plate containing a preexisting crack with the gradient direction of 30° is performed in Fig. 13. Trajectories of main crack initiated from the pre-existing crack tip are deviated from the central horizontal axis, as shown in Fig. 13(a)-Fig. 13(b). As the dynamic tensile loads continue to apply, two main crack branches occur in the FGMs plates, and some micro-branches can be also observed, as shown in Fig. 13(c)-Fig. 13(d).

When the gradient directional angle is equal to 45°, the main crack growth path initiated from the pre-existing crack tip is almost straight (see Fig. 14(a)-Fig. 14(b)), and the main crack split into two branches in the center of FGMs plate at $t = 100$ μs, as shown in Fig. 14(c). It can be observed from Fig. 14(c) that the upper crack branching angle is smaller than the lower crack branching angle in the FGMs plate under the dynamic loading conditions. Furthermore, the upper crack branch split into multiple crack branches, which also propagates to the right boundary, when the dynamic loads continue to apply, as shown in Fig. 14(d).

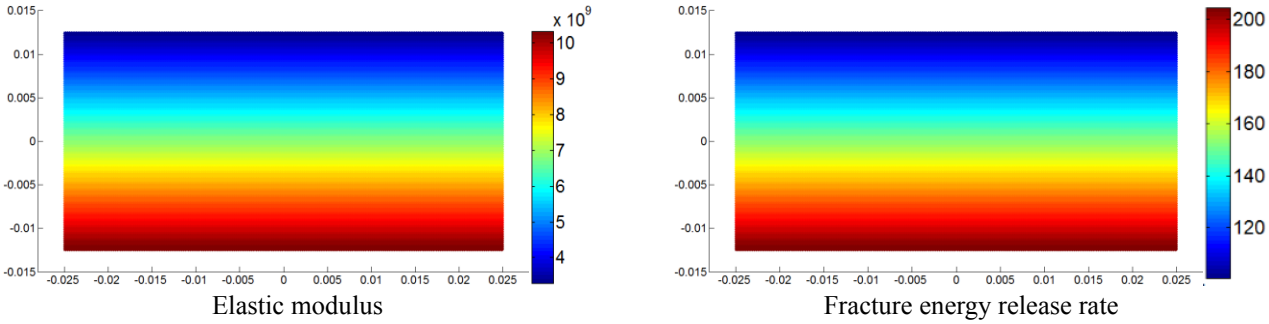

Elastic modulus Fracture energy release rate

(a) Gradient directional angle 0°

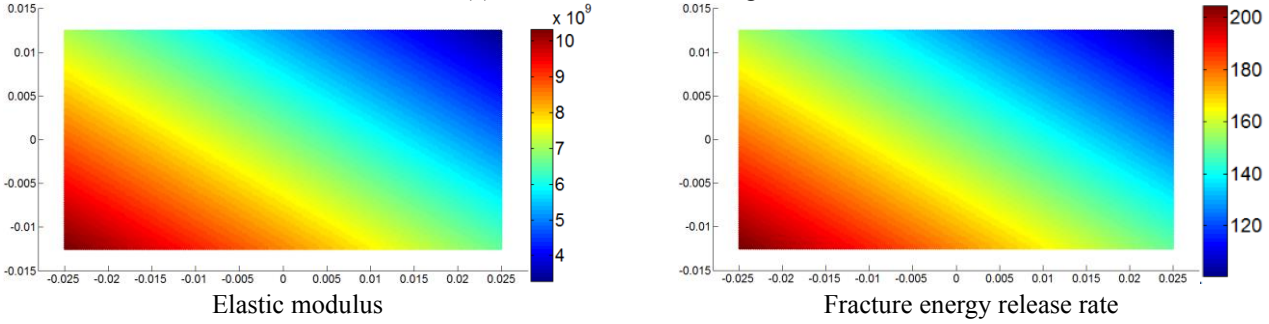

Elastic modulus Fracture energy release rate

(b) Gradient directional angle 30°

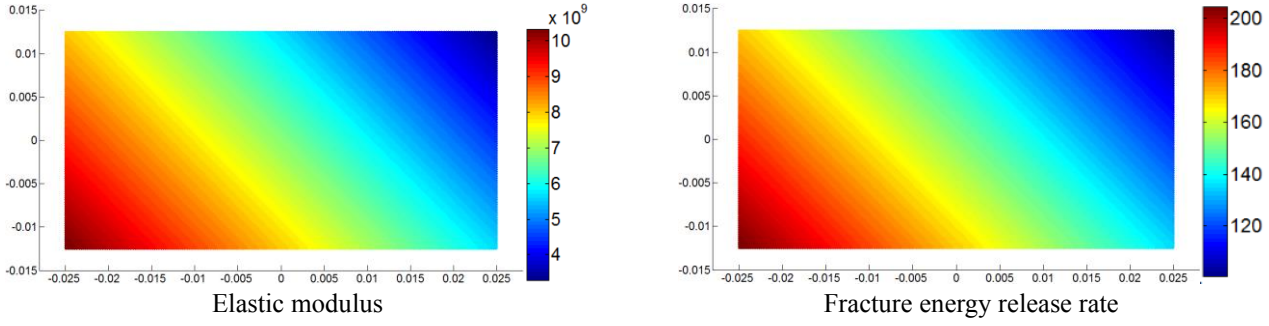

Elastic modulus Fracture energy release rate

(c) Gradient directional angle 45°

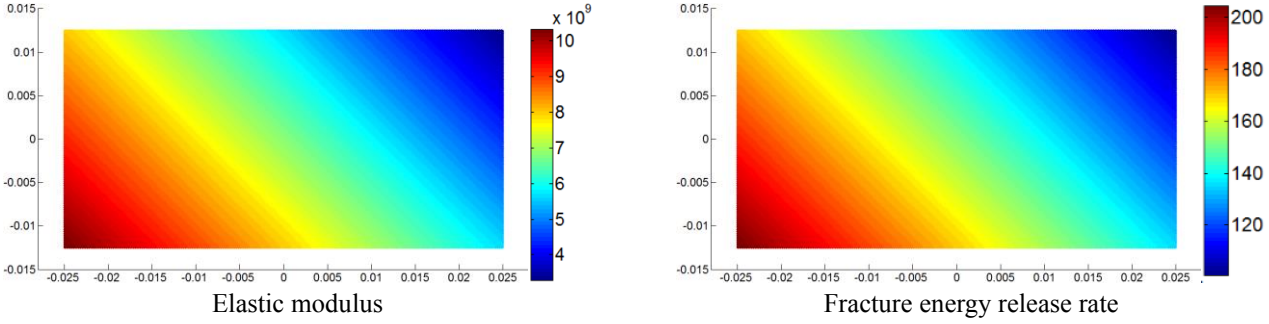

Elastic modulus Fracture energy release rate

(d) Gradient directional angle 60°

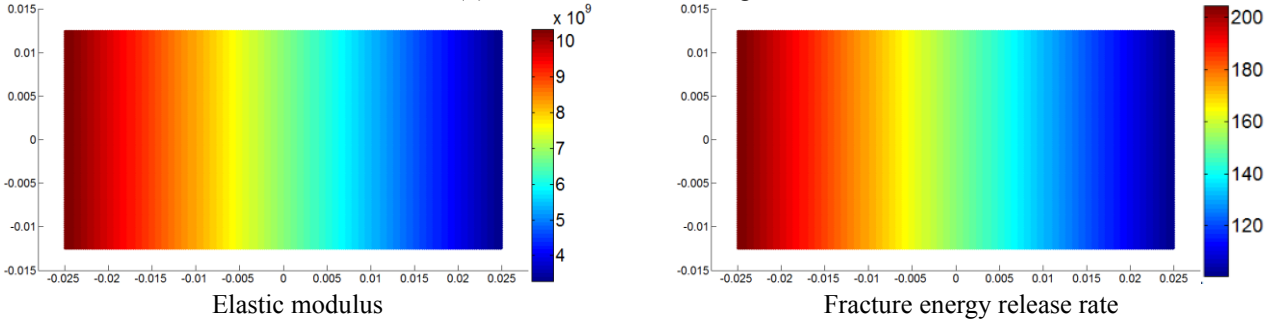

Elastic modulus Fracture energy release rate

(e) Gradient directional angle 90°

Fig. 11 Numerical models FGMs plates with different gradient directions

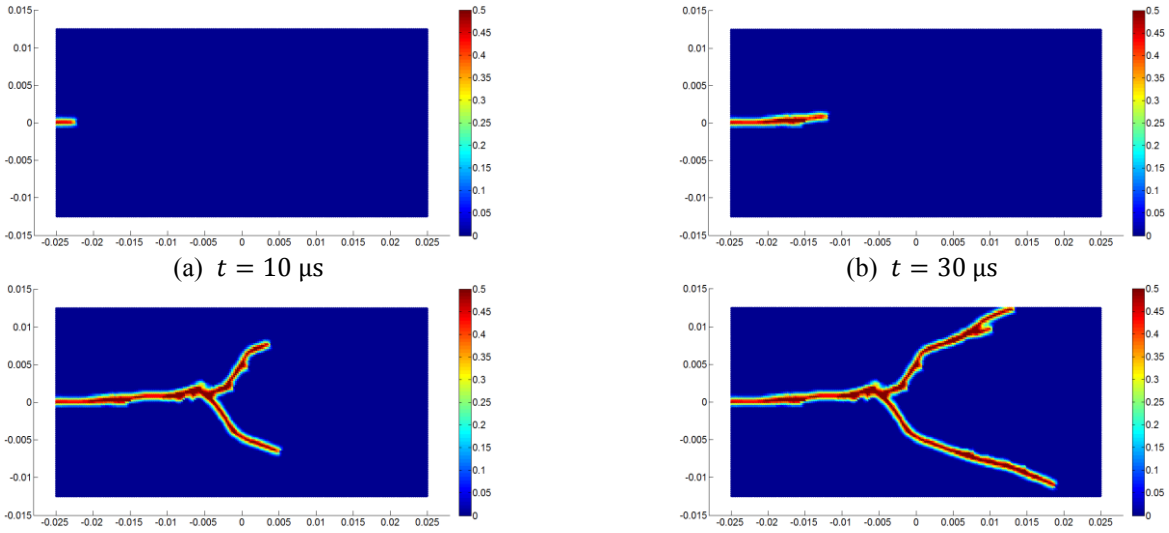

(a) $t = 10$ μs (b) $t = 30$ μs

(c) $t = 60$ μs (d) $t = 80$ μs

Fig. 12 Dynamic fracturing process of FGMs plate with the gradient direction of 0°

When the gradient directional angle is equal to 60°, the

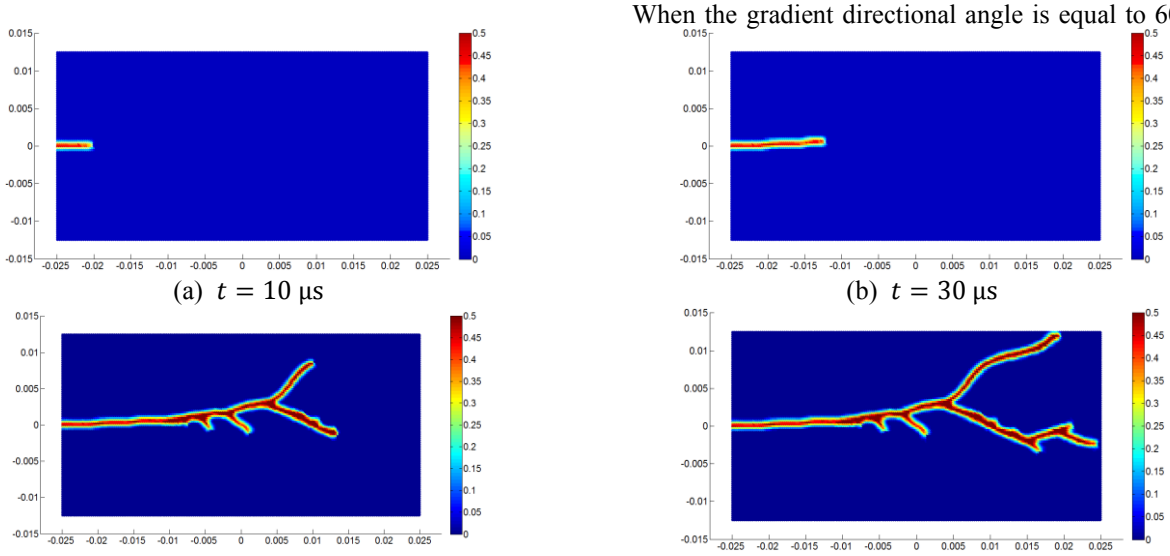

(a) $t = 10$ μs (b) $t = 30$ μs

(c) $t = 60$ μs (d) $t = 80$ μs

Fig. 13 Dynamic fracturing process of FGMs plates with the gradient direction of 30°

main crack is first initiated from the pre-existing crack tip,

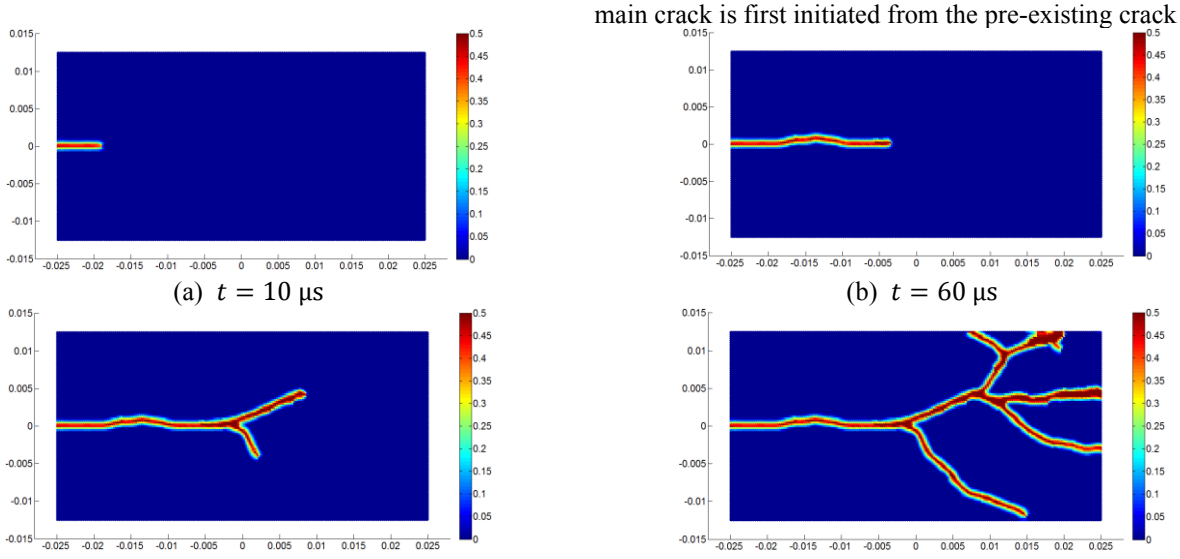

(a) $t = 10$ μs (b) $t = 60$ μs

(c) $t = 100$ μs (d) $t = 120$ μs

Fig. 14 Dynamic fracturing process of FGMs plates with the gradient direction of 45°

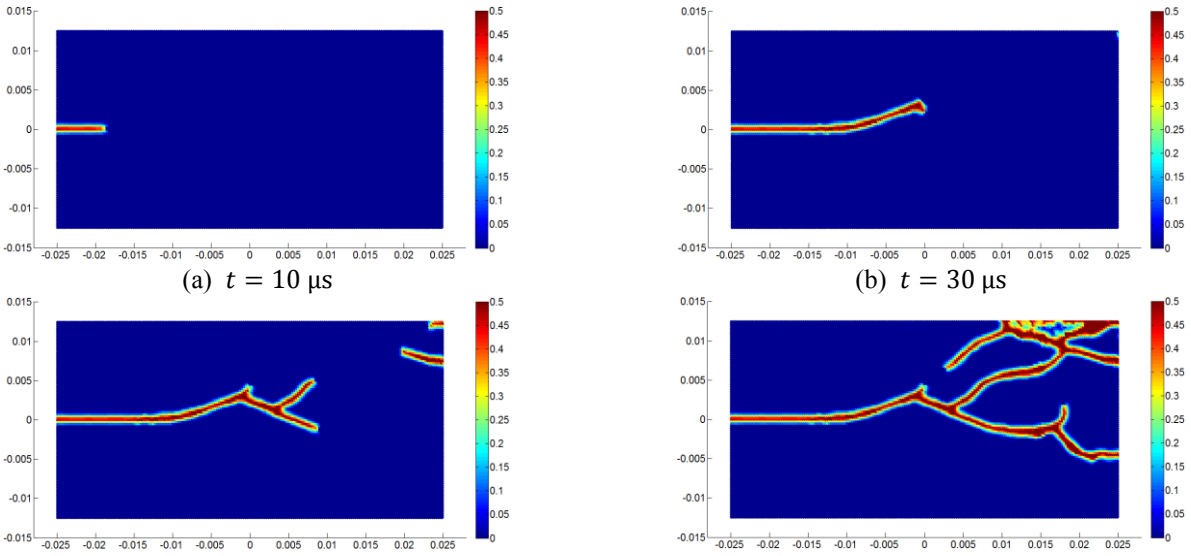

(a) $t = 10$ μs (b) $t = 30$ μs

(c) $t = 60$ μs (d) $t = 80$ μs

Fig. 15 Dynamic fracturing process of FGMs plates with the gradient direction of 60°

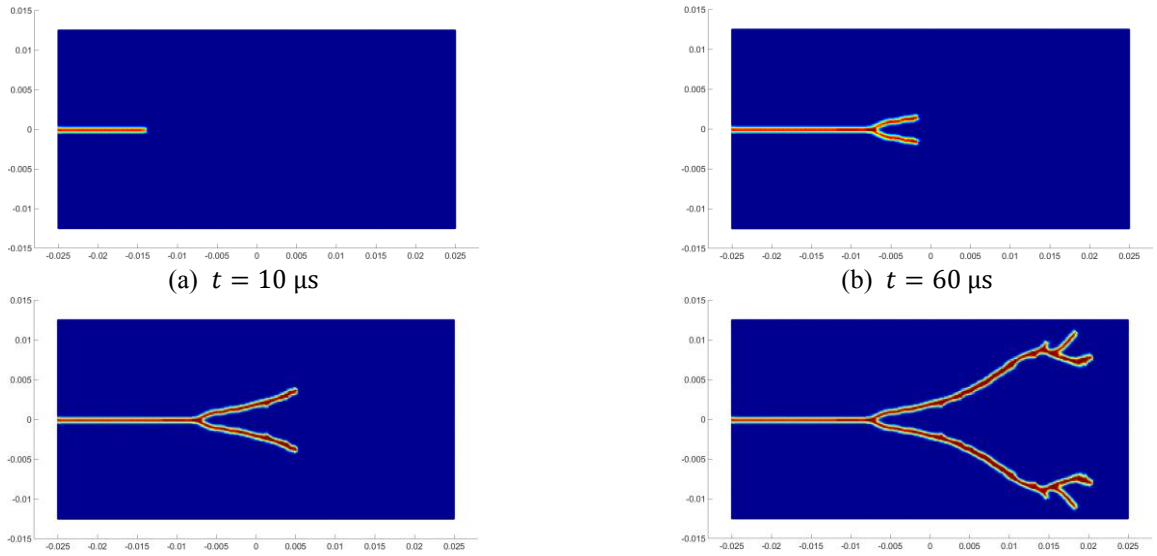

(a) $t = 10$ μs (b) $t = 60$ μs

(c) $t = 80$ μs (d) $t = 100$ μs

Fig. 16 Dynamic fracturing process of FGMs plates with the gradient direction of 90°

and propagates along the horizontal direction at $t = 30$ μs, as shown in Fig. 15(a). When the dynamic loads continue to apply on the upper and lower boundaries, the main crack propagates along the deflective direction, which is towards the compliant parts in FGMs plate at $t = 60$ μs, as shown in Fig. 15(b). When $t = 100$ μs, crack branching occurs at the tip of the main crack, and some cracks appear at the right boundary, which is the compliant part in FGMs plate, as shown in Fig. 15(c). When the dynamic loads continue to apply on the upper and lower boundaries, crack branches appearing from the main crack coalesce with the cracks initiated from the compliant boundary, which leads to the final failure of the FGMs plate, as shown in Fig. 15(d). Similar phenomenon can be observed in the FGMs plate with gradient direction of 90°, as shown in Fig. 16. Furthermore, to investigate the convergence and stability of the developed bond-based peridynamics for FGMs plate, four different numerical samples of the FGMs plate with gradient direction of 60° are simulated for the δ-convergence study. The results of the δ-convergence study are presented in the Appendix.

4.3 Influence of gradient direction on dynamic fracture behaviors

The final crack growth paths in FGMs plates with different gradient directions are shown in Fig. 17. It can be found from Fig. 17(a)-Fig. 17(c) that when the gradient directional angle increases from 0° to 45°, crack growth paths of crack braches are easy to occur in the compliant parts in FGMs plates. Furthermore, it can be also observed from Fig. 17(a)-Fig. 17(c) that the multiple crack braches are more likely to appear as the inclination angle of gradient direction increases. When the gradient directional angle increases to 60°, multiple crack branches initiated from the main crack coalesce with the cracks initiated from the

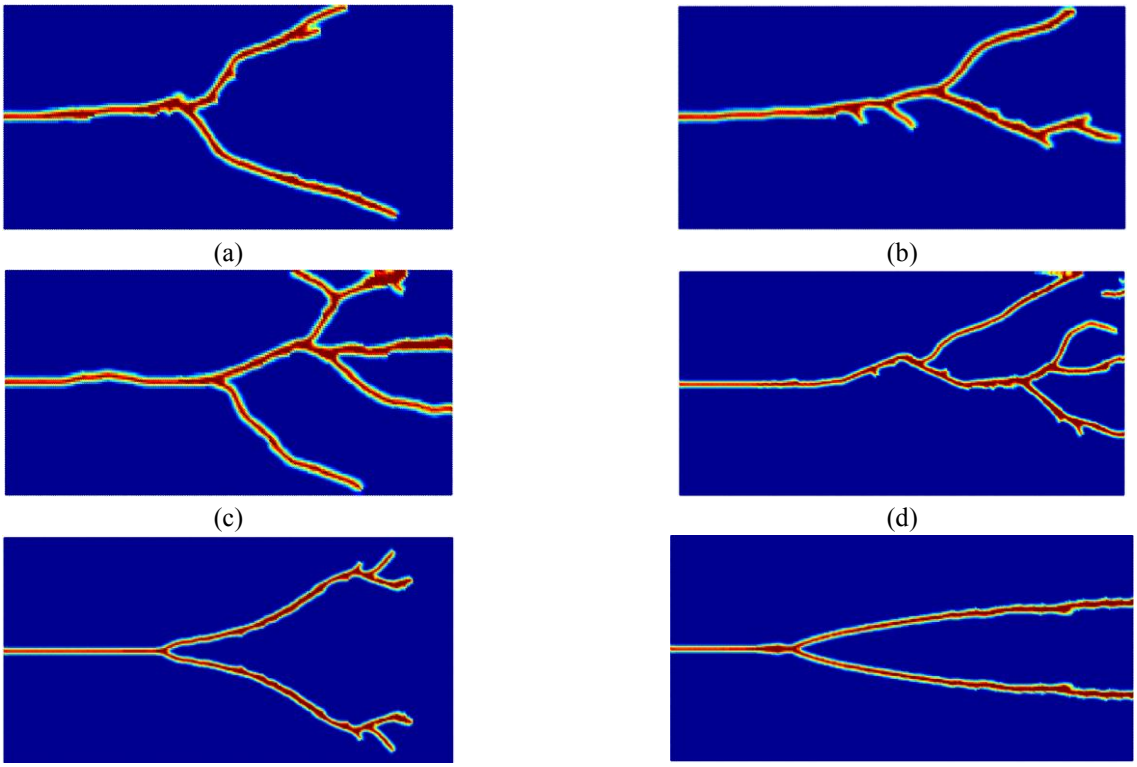

Fig. 17 The final crack growth paths in FGMs plates with different gradient directions: (a) 0°; (b) 30°; (c) 45°; (d) 60°; (e) 90° and (f) homogeneous materials.

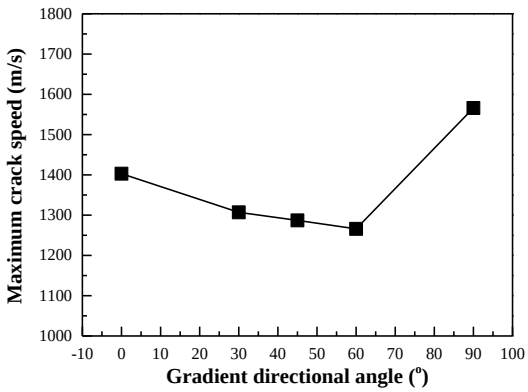

Fig. 18 The directional influence on the maximum crack tip velocity in the FGMs plates under dynamic loading conditions

compliant boundaries, as shown in Fig. 17(d). Similar phenomenon can be observed in the FGM plate with the gradient directional angle of 90°, as shown in Fig. 17(e). It can be found from Fig. 17(e) and Fig. 17(f) that the symmetrical characteristics of geometrics, material properties and loading conditions result in the symmetrical crack growth paths in FGMs plates under the dynamic loading conditions.

Fig 18 shows the influence of gradient direction on the maximum crack tip velocity in the FGMs plates subjected to the dynamic loads. It can be found from Fig. 18 that the gradient direction in the FGMs plates under the dynamic loading conditions significantly affects the maximum crack tip velocity. When the inclination angle of gradient direction increases from 0° to 60°, the maximum crack tip velocity gradually decreases, as shown in Fig. 18. While, as shown in Fig. 18, when the inclination angle of gradient direction increases from 60° to 90°, the maximum crack tip velocity increases. Moreover, the crack tip velocities in different FGMs and homogenous plates under dynamic loading are less the Rayleigh wave velocity.

5. Conclusions

In this study, the weighted projected technique is implemented into the developed bond-based peridynamic model, where bonds can be classified into transverse directionally peridynamic bond, gradient directionally peridynamic bond and arbitrary directionally peridynamic bond based on the geometrical relationship between bonded direction and gradient direction, for functionally graded materials (FGMs). The bond-based peridynamic simulation of crack propagation and branching in homogeneous PMMA plates under dynamic loading conditions are first compared with the previous experimental observations and the previous phase-field results. The present numerical results are in good agreement with the previous experimental and phase-field results. The developed bond-based peridynamics is then applied to investigate the dynamic fracture characteristics in FGMs. Moreover, effects of initial crack length and gradient direction of FGMs on dynamic fracture behaviors are numerically investigated.

Some dynamic fracture characteristics of FGMs subjected to dynamic loads are drawn as follows:

- The developed bond-based peridynamics can effectively reproduce the dynamic fracture phenomenon in the brittle FGMs.
- The dynamic crack growth paths in homogeneous PMMA plates under dynamic loading perform to be symmetrical. While, the dynamic crack growth paths in FGMs subjected to dynamic loads show to be nonsymmetrical.
- For the influence of gradient directions on dynamic crack growth paths in FGMs plates under dynamic loading, multiple crack braches and some boundary cracks are likely to appear in the compliant parts of FGMs, as the gradient directional angle increases.

For the effect of gradient direction on crack propagation velocities in FGMs plates subjected to dynamic loads, the maximum crack tip velocity first decreases, then increases with the increase of the gradient directional angle.

Acknowledgment

This work was financially supported by Project funded by China Postdoctoral Science Foundation (Grant No. 2020M672017), National Program on Key Basic Research Project (Grant No. 2018YFC1505300-1), National Natural Science Foundation of China (Grant Nos. 51674151 and 51704173). Furthermore, Yunteng Wang wants to express his memory of his maternal grandfather, Mr. Jie-Zhi Yan, who always gives him encouragement in academics.

References

Abanto-Bueno, J. and Lambros, J. (2006), "An experimental study of mixed model crack initiation and growth in functionally graded materials", *Exp. Mech.,* **46**(2), 179-186. https://doi.org/10.1007/s11340-006-6416-6.

Aizikovich, S.M., Galybin, A.N. and Krenev, L.I. (2015), "Semi-analytical solution for mode I penny-shaped crack in a soft inhomogeneous layer", *Int. J. Solids Struct.,* **53**, 129-137. https://doi.org/10.1016/j.ijsolstr.2014.10.010.

Arefi, M. (2015), "Elastic solution of a curved beam made of functionally graded materials with different cross sections", *Steel Compos. Struct.,* **18**(3), 659-672. https://doi.org/10.12989/scs.2015.18.3.659.

Areias, P., Rabczuk T. and Dias-da –Costa, D. (2013), "Element-wise fracture algorithm based on rotation of edges", *Eng. Fract. Mech.,* **110**, 113-137. https://doi.org/10.1016/j.engfracmech.2013.06.006.

Areias, P., Msekh M. and Rabczuk, T. (2016), "Damage and fracture algorithm using the screened poisson equation and local remeshing", *Eng. Fract. Mech.,* **158**, 116-143. https://doi.org/10.1016/j.engfracmech.2015.10.042.

Areias, P., Reinoso, J., Camanho, P., Cesar de Sa, J. and Rabczuk T. (2018), "Effective 2D and 3D crack propagation with local mesh refinement and the screened Poisson equation", *Eng. Fract. Mech.,* **189**, 339-360. https://doi.org/10.1016/j.engfracmech.2017.11.017.

Arioui, O., Belakhdar, K., Kaci, A. and Tounsi, A. (2018), "Thermal buckling of FGM beams having parabolic thickness variation and temperature dependent materials", *Steel Compos. Struct.,* **27**(6), 777-788. https://doi.org/10.12989/scs.2018.27.6.777.

Bazazzadeh, S., Shojaei, A., Zaccariotto, M. and Galvanetto, U. (2018), "Application of the Peridynamic differential operator to the solution of sloshing problems in tanks", *Eng. Comput.,* **36**(1), 45-83. https://doi.org/10.1108/EC-12-2017-0520.

Bazazzadeh, S., Mossaiby, F. and Shojaei, A. (2020), "An adaptive thermo-mechanical peridynamic model for fracture analysis in ceramics", *Eng. Fract. Mech.,* **223**, 106708. https://doi.org/10.1016/j.engfracmech.2019.106708.

Bobaru, F. and Duangpanya, M. (2010), "The peridynamic formulation for transient heat conduction", *Int. J. Mass Transf.,* **53**(19), 4047-4059. https://doi.org/10.1016/j.ijheatmasstransfer.2010.05.024.

Bobaru, F. and Hu, W. (2012), "The meaning selection and use of the peridynamic horizon and its relation to crack branching in brittle materials", *Int. J. Fract.,* **176**(2), 215-222. https://doi.org/10.1007/s10704-012-9725-z.

Bobaru, F. and Duangpanya, M. (2012), "A peridynamic formulation for transient heat conduction in bodies with evolving discontinuities", *J. Comput. Phys.,* **231**(**7**), 2764-2785. https://doi.org/10.1016/j.jcp.2011.12.017.

Bourdin, B., Francfort, G. and Marigo, J.J. (2000), "Numerical experiments in revisited brittle fracture", *J. Mech. Phys. Solids,* **48**(4), 797-826. https://doi.org/10.1016/s0022-5096(99)00028-9.

Bouiadjra, R.B., Mahmoudi, A., Benyoucef, S., Tounsi, A. and Bernard, F. (2018), "Analytical investigation of bend ing response of FGM plate using a new quasi 3D shear deformation theory: Effect of the micromechanical models", *Struct. Eng. Mech.,* **66**(3), 317-328. https://doi.org/10.12989/sem.2018.66.3.317

Carlsson, J. and Isaksson, P. (2019), "Crack dynamics and crack tip shielding in a material containing pores ana lysed by a phase field method", *Eng. Fract. Mech.,* **206**, 526-540. https://doi.org/10.1016/j.engfracmech.2018.11.013.

Cheng, Z.Q., Gao, D.Y. and Zhong, Z. (2012), "Interface crack of two dissimilar bonded functionally graded strips with arbitrary distributed properties under plane deformations", *Int. J. Mech. Sci.,* **54**(1), 287-293. https://doi.org/10.1016/j.ijmecsci.2011.11.009.

Cheng, Z., Liu, Y., Zhao, J., Feng, H. and Wu, Y. (2018), "Numerical simulation of crack propagation and branching in functionally graded materials using peridynamic modeling", *Eng. Fract. Mech.,* **191**, 13-32. https://doi.org/10.1016/j.engfracmech.2018.01.016.

Cheng, Z.Q., Sui, Z.B., Cheng, H., Yuan, C.F. and Chu, L.S. (2019), "Studies of dynamic fracture in functionally graded materials usingperidynamic modeling with composite weighted bond", *Theor. Appl. Fract. Mech.,* **103**, 102242. https://doi.org/10.1016/j.tafmec.2019.102242.

Cheng, Z., Zhang, G., Wang, Y. and Bobaru, F. (2015), "A peridynamic model for dynamic fracture in functionally graded materials", *Compos. Struct.,* **133**, 529-546. https://doi.org/10.1016/j.compstruct.2015.07.047.

Chen, Z., Niazi, S. and Bobaru, F. (2019), "A peridynamic model for brittle damage and fracture in porous materi als", *Int. J. Rock Mech. Min. Sci.*, **122**, 104059. https://doi.org/10.1016/j.ijrmms.2019.104059.

Chen, Z. and Bobaru, F. (2015), "Peridynamic modeling of pitting corrosion damage", *J. Mech. Phys. Solids,* **78**, 352-381. https://doi.org/10.1016/j.jmps.2015.02.015.

Chen, Z., Bakenhus, D. and Bobaru F. (2016), "A constructive peridynamic kernel for elasticity", *Comput. Methods Appl. Mech. Engrg.,* **311**, 356-373. https://doi.org/10.1016/j.cma.2016.08.012.

Diana, V. and Casolo, S. (2019), "A bond-based micropolar peridynamic model with shear deformability: Elasticity, failure properties and initial yield domains", *Int. J Solids Struct.,* **160**, 201-231. https://doi.org/10.1016/j.ijsolstr.2018.10.026.

Fallahnejad, M., Bagheri, R. and Noroozi, M. (2018), "Transient analysis of two dissimilar FGM layers with mul tiple interface cracks", *Struct. Eng. Mech.,* **67**(3), 277-281.

https://doi.org/10.12989/sem.2018.67.3.277.
Francfort, G.A. and Marigo, J.J. (1998), "Revisiting brittle fracture as an energy minimization problem", *J. Mech. Phys. Solids,* **46**(**8**), 1319-1342. https://doi.org/10.1016/s0022-5096(98)00034-9.
Galeban, M.R., Mojahedin, A., Taghavi, Y. and Jabbari, M. (2016), "Free vibration of functionally graded thin beams made of saturated porous materials", *Steel Compos. Struct.,* **21**(5), 999-1016. https://doi.org/10.12989/scs.2016.21.5.999.
Gu, P. and Asaro, R.J. (1997), "Cracks in functionally graded materials", *Int. J. Solids Struct.,* **34**(1), 1-17. https://doi.org/10.1016/0020-7683(95)00289-8.
Gupta, A., Jain, N.K., Salhotra, R. and Joshi, P.V. (2018), "Effect of crack location on vibration analysis of partially cracked isotropic and FGM micro-plate with non-uniform thickness: An analytical approach", *Int. J. Mech. Sci.,* **145**, 410-429. https://doi.org/10.1016/j.ijmecsci.2018.07.015.
Gu, X., Zhang, Q., Huang, D. and Yv, Y. (2016), "Wave dispersion analysis and simulation method for concrete SHPB test in peridynamics", *Eng. Fract. Mech.,* **160**, 124-137. https://doi.org/10.1016/j.engfracmech.2016.04.005.
Ha, Y.D. and Bobaru, F. (2010), "Studies of dynamic crack propagation and crack branching with peridynamics", *Int. J. Fract.,* **162**(**1-2**), 229-244. https://doi.org/10.1007/s10704-010-9442-4.
Ha, Y.D. and Bobaru F. (2011), "Characteristics of dynamic brittle fracture captured with peridynamics", *Eng. Fract. Mech.,* **78**(6), 1156-1168. https://doi.org/10.1016/j.engfracmech.2010.11.020.
Ha, Y.D., Lee J. and Hong J.W. (2015), "Fracturing patterns of rock-like materials in compression captured with peridynamics", *Eng. Fract. Mech.,* **144**, 176-193. https://doi.org/10.1016/j.engfracmech.2015.06.064.
Huang, D., Lu, G., Wang, C. and Qiao, P. (2015), "An extended peridynamic approach for deformation and fracture analysis", *Eng. Fract. Mech.,* **141**, 196-211. https://doi.org/10.1016/j.engfracmech.2015.04.036.
Huang, D., Lu, G. and Qiao, P. (2015), "An improved peridynamic approach for quasi-static elastic deformation and brittle fracture analysis", *Int. J. Mech. Sci.,* **94-95**, 111-122. https://doi.org/10.1016/j.ijmecsci.2015.02.018.
Hu, Y.L. and Madenci, E. (2016), "Bond-based peridynamic modeling of composite laminates with arbitrary fiber orientation and stacking sequence", *Compos. Struct.,* **153**, 139-175. https://doi.org/10.1016/j.compstruct.2016.05.063.
Hu, Y.L. and Madenci, E. (2017), "Peridynamics for fatigue life and residual strength prediction of composite lam inates", *Compos. Struct.,* **160**, 169-184. https://doi.org/10.1016/j.compstruct.2016.10.010.
Hu, Y.L., Madenci, E. and Phan, N. (2017), "Peridynamics for predicting damage and its growth in composites", *Fatigue Fract. Eng. Mater. Struct.,* **40**(8), 1214-1226. https://doi.org/10.1111/ffe.12618.
Jin, X., Wu, L.Z., Guo, L.C., Yu H.J. and Sun Y.G. (2009), "Experimental investigation of the mixed-mode crack propagation in ZrO2/NiCr functionally graded materials", *Eng. Fract. Mech.,* **76**(12), 1800-1810. https://doi.org/10.1016/j.engfracmech.2009.04.003.
Kirugulige, M.S. and Tippur H.V. (2006), "Mixed-mode dynamic crack growth in functionally graded glass-filled epoxy", *Exp. Mech.,* **46**(2), 269-281. https://doi.org/10.1007/s11340-006-5863-4.
Kou, M., Han, D., Xiao, C. and Wang Y. (2019a), "Dynamic fracture instability in brittle materials: Insights from DEM simulations", *Struct. Eng. Mech.,* **71**(1), 65-75. https://doi.org/10.12989/sem.2019.71.1.065.
Kou, M.M., Lian, Y.J. and Wang, Y.T. (2019b), "Numerical investigations on crack propagation and crack branching in brittle solids under dynamic loading using bond-particle model", *Eng. Fract. Mech.,* **212**, 41-56. https://doi.org/10.1016/j.engfracmech.2019.03.012.
Kou, M., Liu, X., Tang, S., and Wang, Y. (2019c), "3-D X-ray computed tomography on failure characteristics of rock-like materials under coupled hydro-mechanical loading", *Theor. Appl. Fract. Mech.,* **104**, 102396. https://doi.org/10.1016/j.tafmec.2019.102396.
Lee, J., Hong, J.W. and Jung, J.W. (2017), "The mechanism of fracture coalescence in pre-cracked rock-type mate rial with three flaws", *Eng. Geol.,* **223**, 31-47. https://doi.org/10.1016/j.enggeo.2017.04.014.
Le, Q.V., Chan, W.K. and Schwartz, J. (2014), "A two-dimensional ordinary, state based peridynamic model for linearly elastic solids", *Int. J. Numer. Meth. Engng.*, **98**(8), 547-561. https://doi.org/10.1002/nme.4642.
Luo, J., Ramazani, A. and Sundararaghavan, V. (2018), "Simulation of micro-scale shear bands using peridynamics with an adaptive dynamic relaxation method", *Int. J. Solids Struct.,* **130-131**, 36-48.
Luo, J. and Sundararaghavan, V. (2018), "Stress-point method for stabilizing zero–energy modes in non–ordinary state–based peridynamics", *Int. J. Solids Struct.,* **150**, 197-207. https://doi.org/10.1016/j.ijsolstr.2018.06.015.
Messaoudi, K., Boukhalfa, A. and Beldjelili, Y. (2018), "Three dimensional finite elements modeling of FGM plate bending using UMAT", *Struct. Eng. Mech.,* **66**(4), 487-494. https://doi.org/10.12989/sem.2018.66.4.487.
Moës, N., Dolbow, J. and Belytschko, T. (1999), "A finite element method for crack growth without remeshing", *Int. J. Numer. Meth. Engng.,* **46**(1), 131-150. https://doi.org/10.1002/(SICI)1097-0207(19990910)46:1<131::AID-NME726>3.0.CO;2-J.
Moës, N. and Belytschko, T. (2002), "Extended finite element method for cohesive crack growth", *Eng. Fract. Mech.,* **69**(7), 813-833. https://doi.org/10.1016/s0013-7944(01)00128-x.
Miehe, C., Hofacker, M. and Welschinger, F. (2010), "A phase field model for rate-independent crack propagation: robust algorithmic implementation based on operator splits", *Comput. Methods Appl. Mech. Engrg.,* **199**, 2765-2778. https://doi.org/10.1016/j.cma.2010.04.011.
Nabil, B., Abdelkader, B., Miloud, A. and Noureddine, B. (2017), "On the mixed-mode crack propagation in FGMs plates: comparison of different criteria", *Struct. Eng. Mech.,* **61**(3), 371-379. https://doi.org/10.12989/sem.2017.61.3.371.
Nguyen, D.K. and Tran, T.T. (2018), "Free vibration of tapered BFGM beams using an efficient shear deformable finite element model", *Steel Compos. Struct.,* **29**(3), 363-377. https://doi.org/10.12989/scs.2018.29.3.363.
Ni, T., Zhu, Q.Z., Zhao, L.Y. and Li, P.F. (2018), "Peridynamic simulation of fracture in quasi brittle solids using irregular finite element mesh", *Eng. Fract. Mech.,* **188**, 320-343. https://doi.org/10.1016/j.cma.2018.11.028.
Ni, T., Zaccariotto, M., Zhu, Q.Z. and Galvanetto, U.(2019), "Static solution of crack propagation problems in peri dynamics", *Comput. Methods Appl. Mech. Engrg.,* 346, 126-151. https://doi.org/10.1016/j.cma.2018.11.028.
Pan, H.Z., Song, T.S. and Wang, Z.H. (2015), "An analytical model for collinear cracks in functionally graded materials with general mechanical properties", *Compos. Struct.,* **132**, 359-371. https://doi.org/10.1016/j.compstruct.2015.05.055.
Park, W.T., Han, S.C. and Jung, W.Y. (2016), "Dynamic instability analysis for S-FGM plates embedded in Paster nak elastic medium using the modified couple stress theory", *Steel Compos. Struct.,* **22**(6), 1239-1259. https://doi.org/10.12989/scs.2016.22.6.1239.
Rabczuk, T. and Belytschko, T. (2004), "Cracking particles: a simplified meshfree method for arbitrary evolving cracks", *Int. J.*

Numer. Meth. Engng., **61**(13), 2316-2343. https://doi.org/10.1002/nme.1151.

Rabczuk, T. and Belytschko, T. (2007), "A three-dimensional large deformation meshfree method for arbitrary evolving cracks", Comput. Methods Appl. Mech. Engrg., **196**(29-30), 2777-2799. https://doi.org/10.1016/j.cma.2006.06.020.

Rabczuk, T. and Zi, G. (2007), "A meshfree method based on the local partition of unity for cohesive cracks", *Comput. Mech.,* **39**(**6**), 743-760. https://doi.org/10.1007/s00466-006-0067-4.

Ren, H.L., Zhuang, X.Y., Cai, Y.C. and Rabczuk T. (2016), "Dual-horizon peridynamics", *Int. J. Numer. Meth. Engng.,* **108**(12), 1451-1476. https://doi.org/10.1002/nme.5257.

Ren, H.L., Zhuang, X.Y. and Rabczuk, T. (2017), "Dual-horizon peridynamics: A stable solution to varying hori zons", *Comput. Methods Appl. Mech. Engrg.,* **318**, 762-782. https://doi.org/10.1016/j.cma.2016.12.031.

Rousseau, C.E. and Tippur H.V. (2001), "Dynamic fracture of compositionally graded materials with cracks along the elastic gradient: experiments and analysis", *Mech. Mater.,* **33**(7), 403-421. https://doi.org/10.1016/s0167-6636(01)00065-5.

Shojaei, A., T., Zaccariotto, M. and Galvanetto, U. (2016), "A coupled meshless finite point/Peridynamic method for 2D dynamic fracture analysis", *Int. J. Mech. Sci.,* **119**, 419-431. https://doi.org/10.1016/j.ijmecsci.2016.11.003.

Shojaei, A., Mossaiby, F., Zaccariotto, M. and Galvanetto, U. (2018), "An adaptive multi-grid peridynamic method for dynamic fracture analysis", *Int. J. Mech. Sci.,* **144**, 600-617. https://doi.org/10.1016/j.ijmecsci.2018.06.020.

Shojaei, A., Galvanetto, U., Rabczuk, T., Jenabi, A. and Zaccariotto, M. (2019a), "A generalized finite difference method based on the Peridynamic differential operator for the solution of problems in bounded and unbounded domains", *Comput. Methods Appl. Mech. Engrg.,* **343**, 100-126. https://doi.org/10.1016/j.cma.2018.08.033.

Shojaei, A., Mossaiby, F., Zaccariotto, M. and Galvanetto, U., (2019b), "A local collocation method to construct Dirichlet-type absorbing boundary conditions for transient scalar wave propagation problems", *Comput. Methods Appl. Mech. Engrg.,* **356**, 629-651. https://doi.org/10.1016/j.cma.2019.07.033.

Mossaiby, F., Shojaei, A., Boroomand, B., Zaccariotto, M. and Galvanetto, U. (2020), "Local Dirichlet-type absorbing boundary conditions for transient elastic wave propagation problems", *Comput. Methods Appl. Mech. Engrg.,* **362**, 112856. https://doi.org/10.1016/j.cma.2020.112856.

Silling, S.A. (2000), "Reformulation of elasticity theory discontinuities and long range force", *J. Mech. Phys. Solids,* **48**(1), 175-209. https://doi.org/10.1016/s0022-5096(99)00029-0.

Silling, S.A. and Askari, E. (2005), "A meshfree method based on the peridynamic model of solid mechanics", *Comput. Struct.,* **83**(17), 1526-1535. https://doi.org/10.1016/j.compstruc.2004.11.026.

Silling, S.A., Epton, M., Weckne, O., Xu, J. and Askari, E. (2007), "Peridynamic states and constitutive modeling", J. Elast., **88**(2), 151-184. https://doi.org/10.1007/s10659-007-9125-1.

Silling, S.A. (2014), "Origin and effect of nonlocality in a composite", *J. Mech. Mater. Struct.,* **9**(2), 245-258. https://doi.org/10.2140/jomms.2014.9.245.

Wang, Y., Zhou, X. and Xu, X. (2016), "Numerical simulation of propagation and coalescence of flaws in rock materials under compressive loads using the extended non-ordinary state-based peridynamics", *Eng. Fract. Mech.,* **163**, 248-273. https://doi.org/10.1016/j.engfracmech.2016.06.013.

Wang, Y., Zhou, X. and Shou, Y. (2017), "The modeling of crack propagation and coalescence in rocks under uni axial compression using the novel conjugated bond-based peridynamics", *Int. J. Mech. Sci.,* **128-129**, 614-643. https://doi.org/10.1016/j.ijmecsci.2017.05.019.

Wang, Y., Zhou, X., Wang, Y. and Shou, Y. (2018a), "A 3-D conjugated bond-pair-based peridynamic formulation for initiation and propagation of cracks in brittle solids", *Int. J. Solid Struct.,* **134**, 89-115. https://doi.org/10.1016/j.ijsolstr.2017.10.022.

Wang, Y., Zhou, X. and Kou, M. (2018b), "A coupled thermo-mechanical bond-based peridynamics for simulating thermal cracking in rocks", *Int. J. Fract.*, **211**(1-2), 13-42. https://doi.org/10.1007/s10704-018-0273-z.

Wang, Y., Zhou, X. and Kou, M. (2018c), "Peridynamic investigation on thermal fracturing behavior of ceramic nuclear fuel pellets under power cycles", *Ceram. Int.,* **44**(10), 11512-11542. https://doi.org/10.1016/j.ceramint.2018.03.214.

Wang, L., Xu, J. and Wang, J. (2018d), "A peridynamic framework and simulation of non-Fourier and nonlocal heat conduction", *Int. J. Mass Transf.,* **118**, 1284-1292. https://doi.org/10.1016/j.ijheatmasstransfer.2017.11.074.

Wang, L., Xu, J., Wang, J. and Karihaloo J. B. (2019a), "A mechanism-based spatiotemporal non-local constitutive formulation for elastodynamics of composites", *Mech. Mater.,* **128**, 105-116.

Wang, L., Xu, J. and Wang, J. (2019b), "The elastodynamics in linearized isotropic stated-based peridynamic material", *J. Elast.,* **137**(2), 157–176. https://doi.org/10.1007/s10659-018-09723-7.

Wang Y., Zhou X. and Kou M. (2019c), "An improved coupled thermo-mechanic bond-based peridynamic model for cracking behaviors in brittle solids subjected to thermal shocks", *Eur. J. Mech. A-Solid,* **73**, 282-305. https://doi.org/10.1016/j.euromechsol.2018.09.007.

Wang, Y.T., Zhou, X.P. and Kou, M.M. (2019d), "Three-dimensional numerical study on the failure characteristics of intermittent fissures under compressive-shear loads", *Acta Geotech.,* **14**(4), 1161-1193. https://doi.org/10.1007/s11440-018-0709-7.

Wang, L. and Wang, J. (2019), "On the invariance of governing equations of current nonlocal theories of elasticity under coordinate and gauge transformations", *J. Elast.,* **137**(2), 237–246. https://doi.org/10.1007/s10659-018-09715-7.

Wang, Y.T. and Zhou, X.P. (2019), "Peridynamic simulation of thermal failure behaviors in rocks subjected to heating from boreholes", *Int. J. Rock Mech. Min. Sci.,* **117**, 31-48. https://doi.org/10.1016/j.ijrmms.2019.03.007.

CC

Appendix

For the FGMs plate with the gradient direction of 60°, four different numerical samples with different material particle distributions are simulated to conduct the δ-convergence. The computational details of the four different numerical samples are listed in Table A1. The ultimate crack growth paths of FGMs plates with the gradient direction of 60° are presented in Fig. A1. It can be observed from Fig. A1 that the dynamic crack growth paths in the FGMs plates are similar as the horizon size decreases. Furthermore, the surface effect gradually decreases with the decrease of the horizon size, as shown in Fig. A1.

Table A1 Computational details of the four numerical FGMs plates

No.	Particle spacing Δ (mm)	Horizon size δ (mm)	Nonlocal ratio m	Numerical of particles
Case-I	0.500	2.000	4.0	100×50
Case-II	0.250	1.000		200×100
Case-III	0.167	0.668		300×150
Case-IV	0.125	0.500		400×200

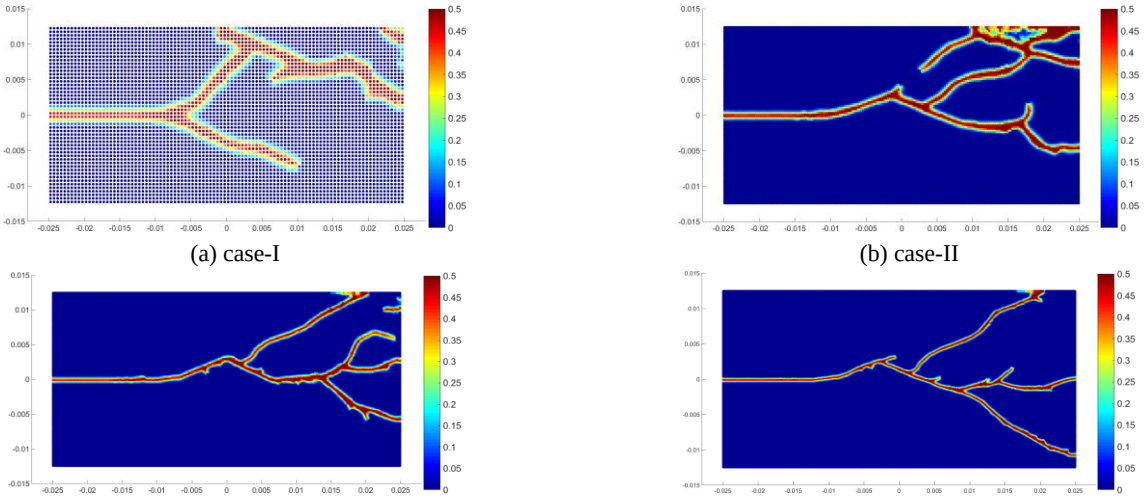

(a) case-I (b) case-II

(c) case-III (d) case-IV

Fig. A1 The ultimately dynamic crack growth paths in the FGMs plates with the gradient direction of 60°.